Journal of Applied Fluid Mechanics, Vol. 19, No. 1, pp. 3335-3353, 2026. Available online at www.jafmonline.net, ISSN 1735-3572, EISSN 1735-3645. https://doi.org/10.47176/jafm.19.1.3632



Performance of a Tube-bundle Heat Exchanger in a Rectangularsection Right-angle Bend Duct

X. Wang, C. Li[†], Y. Yan, and X. Ye

Hebei Key Laboratory of Low Carbon and High-Efficiency Power Generation Technology, North China Electric Power University, Baoding 071003, Hebei, China

†Corresponding Author Email: <u>lichunxi@ncepu.edu.cn</u>

ABSTRACT

Three-dimensional numerical simulations are conducted to elucidate the fundamental differences in hydrodynamics and heat transfer performance between heat exchangers arranged in confined rectangular-section right-angle bend ducts and those in straight ducts, with a specific focus on applications such as gas-quenching furnaces. The effects of the tube-bundle arrangement and number of tube rows on the pressure drop (Δp) and heat-transfer rate (Q) are examined under identical inlet conditions. Based on the performance differences, improved correlations are established for pressure drop and heat transfer performance applicable to rectangular bend ducts. The results demonstrate a definitive ordering of pressure drops: Δp_{ss} (staggered arrangement, straight duct) $> \Delta p_{\rm si}$ (in-line arrangement, straight duct) $> \Delta p_{\rm bi}$ (in-line arrangement, bend duct) $> \Delta p_{\rm bs}$ (staggered arrangement, bend duct), and a parallel hierarchy for heat-transfer rates: $Q_{ss} > Q_{si} > Q_{bi} > Q_{bs}$. Although staggered arrangements achieve only modest heat-transfer gains over in-line arrangements, their marked reduction in pressure drop yields the optimal overall performance evaluation criterion. Both the friction factor f_b and Nusselt number Nu_b of the bend duct increase with the number of tube rows, though their growth attenuates as the tube pitch decreases. These mechanistic insights lead to improved empirical correlations for predicting Δp_b and Nu_b in bend ducts. Validations against simulation data show deviations within $\pm 5\%$, effectively overcoming the limitations of straight-duct formulas in complex bend-duct geometries. These correlations provide a solid theoretical basis for optimizing the design and performance of bend-duct heat exchangers in confined spaces.

Article History

Received April 30, 2025 Revised July 1, 2025 Accepted August 23, 2025 Available online November 5, 2025

Keywords:

Rectangular-section right-angle bend duct Tube-bundle heat exchanger Tube arrangement Heat transfer Pressure drop Improved formulas

1. Introduction

Tube-bundle heat exchangers are widely used in metal heat treatment, energy utilization, and chemical engineering (Dogan, 2025; Moreira et al., 2022; Sang et al., 2025; Yin et al., 2020). In specific gas quenching furnaces used for quenching workpieces, the geometrical limitations of the equipment restrict the heat exchanger design from enabling linear gas flow paths, as demonstrated in the case of the a high-pressure gas quenching furnace (Wang, 2018). Additionally, in single-chamber high-pressure vacuum gas quenching furnaces, space limitations necessitate the arrangement of a gas-cooled tube-bundle heat exchanger within a rectangular-section right-angle bend duct (Hu et al., 2023; Wei, 2013; Wei, et al. 2012). In this configuration, the gas on the shell side flows across the tube-bundle

and undergoes a 90° turn, as shown in Fig. 1. This setup differs significantly from the typical configuration of a tube-bundle heat exchanger within a straight duct. Currently, the empirical formulas used to determine heat transfer and pressure drop for fluids crossing tubebundle arrangements are designed for straight ducts without flow direction changes. For example, the experimental correlation proposed by Zukauskas (Zukauskas, 1986), which is widely used to characterize heat transfer, and the pressure drop correlation recommended by Holman (Holman, 2002), based on Jakob's work (Jakob, 1938), have yet to be validated for rectangular-section right-angle bend ducts. Therefore, it is crucial to investigate the overall performance of tube-bundle heat exchangers arranged in rectangular-section right-angle bend ducts and to elucidate the underlying mechanisms.

Nor	Nomenclature						
D	tube diameter	S_{T}	transverse pitch				
f	friction factor	u_0 $u_{ m max}$	inlet velocity average flow velocity at the minimum flow cross- section of the tube-bundle				
H	height of the model	Greel	c symbols				
$egin{array}{c} L_1 \ L_2 \ L_3 \ L_4 \ \end{array}$	width of the model length of the model inlet section length of the model outlet section length of the model	$\delta \ \mu \ ho$ Subsc	distance from the last row of tubes to the shell wall fluid density dynamic viscosity ripts				
N Nu Pr Δp Q	number of tube rows Nusselt number Prandtl number pressure drop heat-transfer rate	bs bi ss si Abbr	staggered arrangement in the bend duct in-line arrangement in the bend duct staggered arrangement in the straight duct in-line arrangement in the straight duct eviated symbols				
Re S _L	Reynolds number longitudinal pitch	PEC	Performance Evolution Criteria				

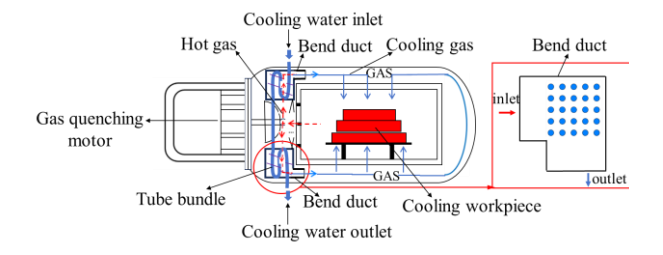


Fig. 1 Schematic diagram of a vacuum gas quenching furnace (Wang, 2018; Wei, et al. 2012)

The published literature on tube-bundle heat exchangers primarily focuses on the influence of the tube arrangement, pitch, number of rows, tube cross-sectional shape, and duct dimensions on the overall performance (Bennour et al. 2024; Deeb 2023; Lang et al. 2024; Liu et al. 2021; Sarangi et al., 2020; Wu et al., 2020; Yang et al., 2022). In the absence of flow direction changes, a staggered arrangement exhibits better heat transfer performance than an in-line arrangement, although in-line arrangements achieve lower flow resistance losses. Overall, staggered configurations demonstrate superior comprehensive performance relative to configurations (Córcoles et al., 2024; Kong et al., 2016; Sakib & Al-Faruk, 2018). The number of tube rows is a key factor influencing the hydrodynamic and heat transfer performance of tube-bundle heat exchangers. Kwak et al. (2003) conducted experiments on the heat transfer and hydrodynamic behaviors of staggered tube bundles and found that, for a constant tube pitch, the number of tube rows has a more significant effect on the hydrodynamics than on the heat transfer. As the number of tube rows increases, the friction coefficient of the tube bundle rises. Zhao et al. (2018) simulated the effects of critical parameters on the performance of rectangular finned elliptical tube exchangers and concluded that the number of tube rows has the most significant impact, followed by the transverse pitch, while the effects of the longitudinal pitch and fin pitch are minimal. Che and Elbel (2021) experimentally examined the heat transfer coefficient of a finned tube heat exchanger with eight rows of tubes, and observed that the heat transfer coefficient gradually

decreases as the number of rows increases, particularly when moving from 1–4 rows. Furthermore, the variation in the heat transfer coefficient at high flow rates is negligible. Moharana et al. (2023) experimentally investigated the effect of the tube row number on the heat transfer performance of staggered configurations under boiling flow conditions, and reported results consistent with those of Che and Elbel (2021).

To explore the underlying hydrodynamic and heat transfer mechanisms in tube-bundle exchangers, extensive studies have explored the interaction between pairs of heat exchange tubes (Derakhshandeh & Alam, 2019; Zdravkovich, 1987; Zheng et al., 2024; Zhou et al., 2009). Their findings indicate that the wake characteristics of the fluid behind the tubes play a critical role in the overall performance of tube-bundle heat exchangers. Key factors influencing the wake characteristics include the Reynolds number, pitch ratio, and tube shape. Several studies have classified the wake behavior behind circular tubes into three distinct regimes based on Reynolds number and pitch ratio (the center-to-center distance, S, of upstream and downstream tubes relative to the tube diameter, D, i.e., S/D: (1) single slender body regime (1.0 < S/D < 1.2–1.8), (2) reattachment regime $(1.2-1.8 \le S/D \le 3.4-3.8)$, and (3) binary vortex street regime (S/D > 3.4-3.8) (Zdravkovich, 1988; Zhang & Melbourne, 1992). Sadeghi et al. (2024) simulated the wake characteristics of two consecutive horizontally placed circular tubes, square tubes, and a combination of circular and square tubes at the Reynolds number of $Re = 3.2 \times 10^4$ with varying pitch ratios. For smaller tube pitches, the drag coefficient of the upstream tube was observed to be higher than that of the downstream tube. As the tube pitch increases, the influence of the upstream tube on the downstream tube diminishes. They identified the critical pitch ratio between the two tubes (i.e., the point at which vortex flow behind the tubes enters the "re-attachment regime") as approximately 3, 3.5, and 4, which aligns with previous findings in the literature (Zdravkovich, 1988; Zhang & Melbourne, 1992). Tsutsui (2010) experimentally investigated the heat transfer characteristics of two consecutive vertically placed circular tubes at Reynolds numbers ranging from $Re = 1.1 \times 10^4$ to $Re = 6.2 \times 10^4$

with different pitch ratios. Their results showed that as the pitch ratio increases, the Nusselt number (Nu) for both tubes decreases, with the upstream tube consistently exhibiting a higher Nu than the downstream tube. Once the pitch ratio reaches a certain threshold, the Nu in both tubes becomes approximately equal and no longer changes.

Additionally, the flow direction is a critical factor influencing the hydrodynamics and heat transfer performance of tube bundles, directly impacting the overall efficiency of heat exchangers. Zhang et al. (2015) experimentally investigated the effect of the attack angle on a tube-bundle heat exchanger and found that both Nu and the drag coefficient increase with the attack angle. Tang et al. (2017) used a porous medium model to conduct both experimental and numerical studies on the hydrodynamics of two-row elliptical finned tube heat exchanger elements at various intake angles (i.e., the angle between the airflow direction and the incoming flow surface of the heat exchanger). The results revealed that the pressure drop is highest at an attack angle of 30°, followed by 45°, and lowest at 90°. At an intake angle of 90°, the flow direction did not change as it passed through the heat exchanger, while at other attack angles, the airflow direction underwent two turns. More recent studies have highlighted the impact of the flow direction. Karabulut (2024) numerically investigated the effects of altering the gas flow direction by introducing baffles at different angles (30°, 60°, and 90°) within the heat exchanger's flow channels. The results showed that both the Nu and Δp were maximized when the baffle angle was 90°. Batista et al. (2025) introduced staggered baffles into the gas flow passages of a heat exchanger, and conducted numerical simulations that demonstrated configuration significantly enhanced heat transfer performance while reducing flow resistance. Na et al. (2025) performed numerical simulations exploring the influence of the tube inclination angle (ranging from 15° to 90°) on heat exchanger performance, and further validated the applicability of existing heat transfer correlations for inclined tubes.

The abovementioned studies highlight that the flow direction within the duct significantly impacts the hydrodynamics and heat transfer performance of tube-

bundle heat exchangers. In particular, when the flow direction changes, especially with a 90° turn, factors such as the tube arrangement (in-line or staggered) and the number of tube rows have substantially different effects from those observed in straight ducts, necessitating further investigation. Moreover, the applicability of empirical formulas for Nu and Δp , developed for straight ducts, to rectangular-section right-angle bend ducts remains unverified. To date, no studies have explored this issue.

To address this gap, the present study develops a geometric model of a tube-bundle heat exchanger situated in a rectangular-section right-angle bend duct, with air flowing across the tube-bundle and undergoing a 90° turn, as encountered in specific gas quenching furnaces. Numerical simulations are employed to examine the effects of the tube arrangement and the number of tube rows on the hydrodynamics and heat transfer performance. By comparing the performance of this configuration with that of a tube-bundle heat exchanger in a straight duct, the underlying causes of performance variations are identified. Building on these findings, improved formulas for Nu and Δp are proposed for tube-bundle heat exchangers in rectangular-section right-angle bend ducts, providing valuable insights for optimizing the performance and structural design of similar heat exchangers.

2. MODEL FORMULATION

2.1 Geometric Model

Based on the application scenario of a specific quenching furnace, a tube-bundle heat exchanger is arranged in a rectangular-section right-angle bend duct (hereinafter referred to as the bend duct), as shown in Fig. 2. The dimensions of the cross-section are as follows: width $L_1 = 646.5$ mm, height H = 743 mm, duct length $L_2 = 578$ mm, inlet section length $L_3 = 300$ mm, outlet section length $L_4 = 300$ mm, and distance from the last row of tubes to the shell wall $\delta = 118$ mm. According to engineering specifications, the duct material of the heat exchanger is aluminum, and the heat exchange tubes inside the shell are copper. The medium inside the tubes is water at 15°C, and the medium outside the tubes is air at

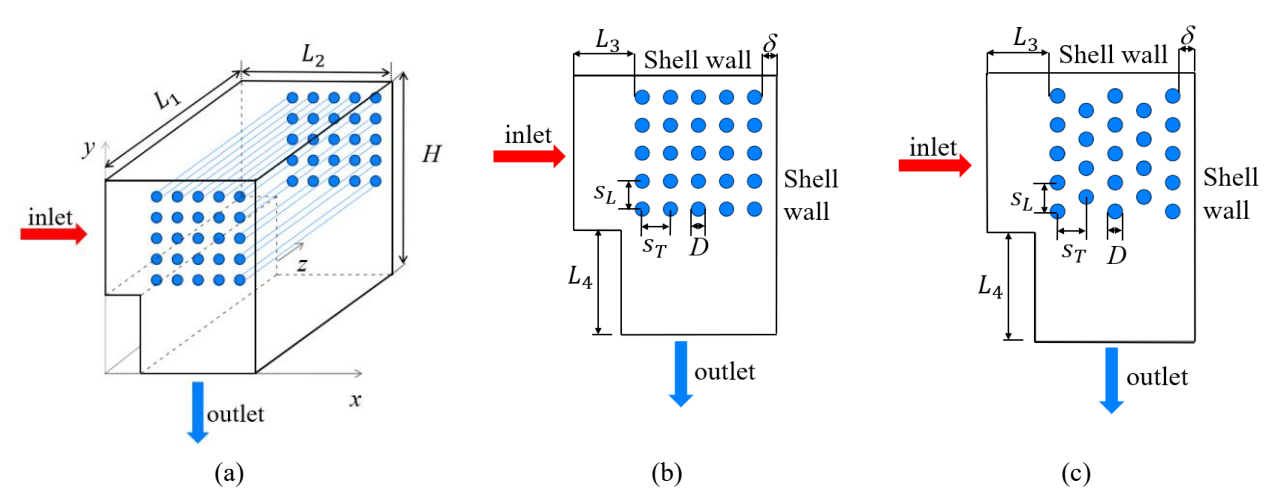


Fig. 2 Schematic diagram of the bend duct model. (a) 3D view of heat exchanger model, (b) in-line arrangement, and (c) staggered arrangement

	Number of tube rows <i>N</i>	Tube arrangements	Total number of tubes	Tube diameter $D(mm)$	Transverse pitch $S_{\rm T}$ (mm)	Longitudinal pitch S _L (mm)
	4×4	In-line	16	40	100	100
		Staggered	14			
Bend duct	5×5	In-line	25	40	80	80
		Staggered	23			
	6×6	In-line	36	40	70	70
		Staggered	33			
Straight	5×5	In-line	25	40	80	80
duct	5×5	Staggered	33	40		

Table 1 Main parameters of the tube-bundle in the bend and straight duct

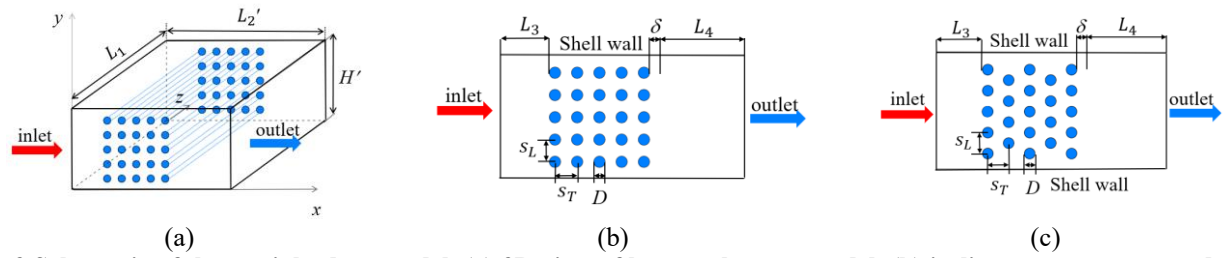


Fig. 3 Schematic of the straight duct model. (a) 3D view of heat exchanger model, (b) in-line arrangement, and (c) staggered arrangement

500°C. Air flows in from the left, passes across the tubebundle heat exchanger, and then exits from the bottom. Based on a three-dimensional geometric model, this study investigates the hydrodynamic and heat transfer performance of the heat exchanger in both in-line (Fig. 2(b)) and staggered arrangements (Fig. 2(c)). Three distinct scenarios are considered for each tube-bundle arrangement, corresponding to 4×4, 5×5, and 6×6 tube row arrangements, as detailed in Table 1.

For comparison, this study also establishes a three-dimensional heat exchanger model with a 5×5 tube-bundle arrangement in a rectangular-section straight duct (i.e., where the air flow does not change direction, hereinafter referred to as the straight duct), as shown in Fig. 3. The straight duct has the same width as the bend duct and a height of H' = 443 mm, which is equal to the inlet height of the bend duct (i.e., $H - L_4$). The tube pitch and tube diameter in the heat exchanger within the straight duct are identical to those in the bend duct. Based on the principle that the overall airflow passage is equal in both the bend and straight ducts, the length of the straight duct is determined as $L'_2 = L_3 + L_4 + 4S_T + 5D + \delta = 878$ mm.

The Fluent meshing software was used to divide the computational domain grid, with the height of the first layer of mesh near the wall set to 2.82×10^{-5} m and the normal grid growth ratio near the wall set to 1.2, to ensure that $y^+ < 1$. To more accurately analyze the hydrodynamics and heat transfer performance within the heat exchanger, the grid resolution in the corners of the heat exchanger model and the tube-bundle section was refined, as shown in Fig. 4.

The inlet boundary condition was set to a velocity inlet. Unless otherwise specified, the velocity values for the eight operating scenarios listed in Table 1 were 10 m/s, 15 m/s, 20 m/s, 25 m/s, 30 m/s, 35 m/s, 40 m/s, and 45 m/s. The turbulence parameters at the inlet were prescribed using the turbulence intensity and hydraulic diameter

method. The turbulence intensity was estimated as a function of the hydraulic diameter and Reynolds number (Pope, 2001). For the eight operating conditions considered in this study, the turbulence intensities were 5.51%, 5.24%, 5.05%, 4.92%, 4.81%, 4.71%, 4.64%, and 4.57%, respectively. The hydraulic diameter was set to 0.04 m. Due to the unchanging velocity and temperature fields, an outflow boundary condition was applied to the outlet. Under the simulated conditions, the gradients of all flow variables (e.g., velocity and temperature) are approximately zero along the streamwise direction. This is a common and appropriate assumption for geometries where the outlet flow behavior is not significantly influenced by downstream conditions, and ensures mass conservation across the entire computational domain. The tube surface was assigned a constant wall temperature of 15°C, maintained by the coolant on the inner surface of the tube. This is supported by two factors: (1) the coolant side possesses a sufficiently high heat transfer coefficient and (2) the coolant flow rate is adequate to maintain an almost uniform tube wall temperature across the entire heat transfer surface. The shell wall was assigned an adiabatic condition. This assumption implies that the heat loss to the external environment through the shell is negligible compared with the dominant heat transfer occurring inside the heat exchanger. These boundary conditions are summarized in Table 2. The pressurevelocity coupling was achieved using the SIMPLEC algorithm, and the convection and diffusion terms were discretized using a second-order upwind scheme. The solution was considered to have converged when the residuals of the continuity and energy equations fell below 10⁻⁶, while the residuals of the momentum and turbulence equations were below 10⁻⁵, with a relative mass flow rate error between inlet and outlet of less than 0.1%.

2.2 Governing Equations

The simulations employed a steady-state computational

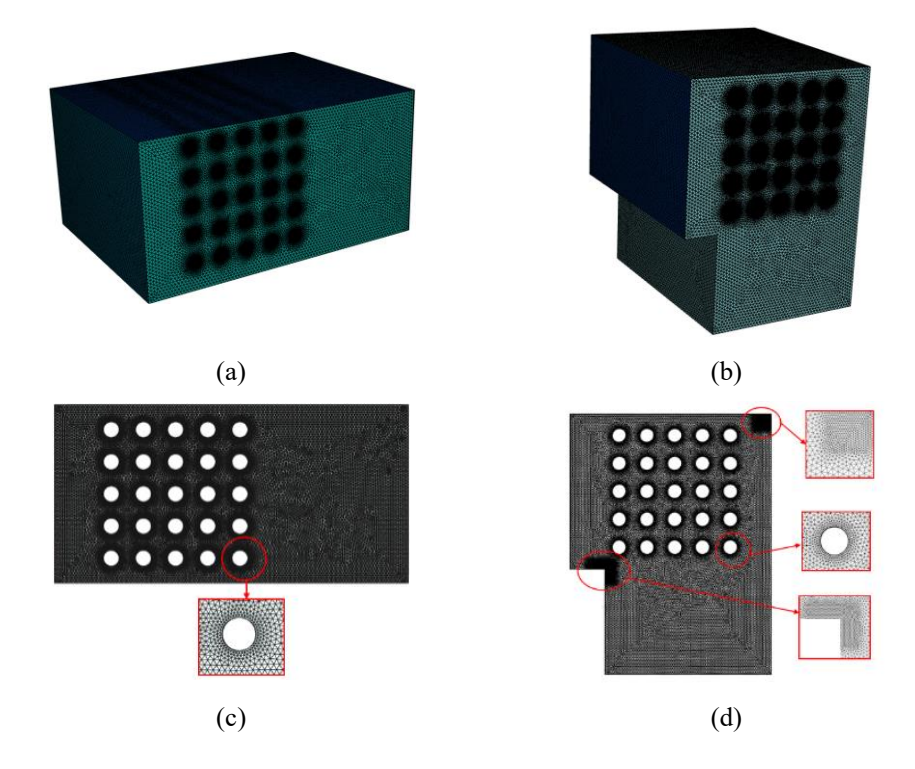


Fig. 4 Schematic of the grid meshing. (a) 3D meshing of straight duct, (b) 3D meshing of bend duct, (c) Local mesh refinement of straight duct, and (d) Local mesh refinement of bend duct

Table 2 Boundary conditions for CFD analysis

Boundary	Boundary conditions	Specific numerical values
Inlet	Velocity-inlet	10 m/s,15 m/s, 20 m/s, 25 m/s, 30 m/s, 35 m/s, 40 m/s, 45 m/s
Outlet	Outflow	
Shell wall	Adiabatic	
Tube surface	Constant wall temperature	15°C

method, assuming an incompressible flow process with gravitational effects neglected and external heat sources (such as radiation) disregarded. The reference temperature was defined as the average of the fluid's inlet and outlet temperatures. Based on these assumptions, the Reynolds average Navier-Stokes method is applied, hence governing equations include continuity, RANS, and energy equations, listed as follows:

$$\frac{\partial(\rho \overline{u}_j)}{\partial x_j} = 0 \tag{1}$$

$$\rho \overline{u}_{j} \frac{\partial \overline{u}_{i}}{\partial x_{j}} = -\frac{\partial \overline{p}}{\partial x_{i}} + \frac{\partial}{\partial x_{j}} \left(\mu \frac{\partial \overline{u}}{\partial x_{j}} - \rho \overline{u'_{i} u'_{j}} \right)$$
 (2)

$$\frac{\partial(\rho \overline{u}_i c_p \overline{T})}{\partial x_i} = \frac{\partial}{\partial x_i} \left(k_{\text{ef}} \frac{\partial \overline{T}}{\partial x_i} \right)$$
 (3)

where ρ is the fluid density; μ is the dynamic viscosity; $\overline{\rho}$ is the time-averaged static pressure; $\rho u_i' u_j'$ represents the Reynolds stress, which indicates the effect of turbulent

pulsation on the time-averaged flow; and $k_{\rm ef} = k + k_{\rm t}$, where $k_{\rm ef}$ represents the effective thermal conductivity, k denotes the laminar thermal conductivity, and $k_{\rm t}$ signifies the turbulent thermal conductivity.

The renormalization group (RNG) k– ε model was employed. This can be written as follows:

$$\frac{\partial(\rho \overline{u}_{j}k)}{\partial x_{j}} = \frac{\partial}{\partial x_{j}} (\alpha_{k} \mu \frac{\partial_{k}}{\partial x_{j}}) + P_{k} - \rho \varepsilon + S_{k}$$
(4)

$$\frac{\partial(\rho \overline{u}_{j}\varepsilon)}{\partial x_{j}} = \frac{\partial}{\partial x_{j}}(\alpha_{\varepsilon}\mu \frac{\partial \varepsilon}{\partial x_{j}}) + C_{\varepsilon 1}\frac{\varepsilon}{k}P_{k} - C_{\varepsilon 2}\rho \frac{\varepsilon^{2}}{k} + S_{\varepsilon}$$
 (5)

where k is the turbulent kinetic energy, ε is the turbulent dissipation rate, P_k is the effective generation rate of k, $C_{\varepsilon 1} = 1.42$, $C_{\varepsilon 2} = 1.68$, and $\alpha_k = \alpha_{\varepsilon} = 1.39$ (empirical coefficient).

2.3 Grid Independence and Model Validation

The grid independence was validated for all eight models presented in Table 1. As an example, a 5×5 in-line arrangement with an inlet velocity of 25 m/s was considered. The average value of Nu on the tube-bundle surface and Δp between the inlet and outlet of the duct were taken as indicators. The simulation results for the straight and bend ducts are illustrated in Fig. 5. When the grid size exceeds 4.36 million cells, the values of Nu and Δp for both ducts remain virtually unchanged, confirming that this grid resolution achieves the required computational accuracy. Considering both computational accuracy and efficiency, a grid size of 4.36 million cells was selected for both models. Through similar grid independence validations, the grid sizes for the models with staggered 5×5 , in-line/staggered 4×4 , and 6×6 tube-

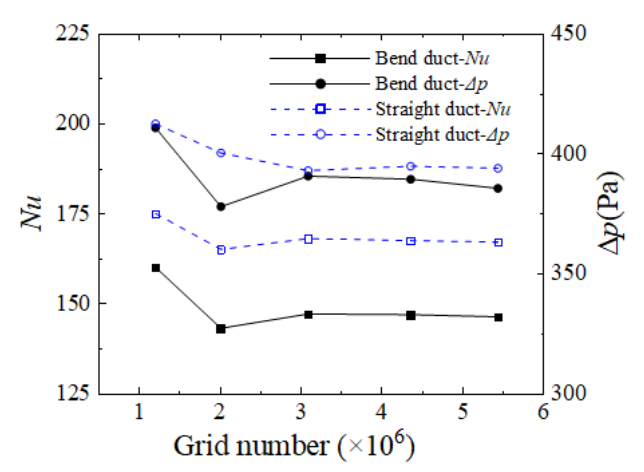


Fig. 5 Grid independence verification

Table 3 Grid independence verification

Bent	Grid	Δp	Nu
duct	size	(Pa)	
	(million)	` /	
	1.21	150.2(-16.1%)	108.5(-15.2%)
4×4	2.35	162.4(-7.9%)	118.4(-5.2%)
in-line	3.53	167.2(-5.2%)	120.3(-7.6%)
in-iine	4.60	179.4(+1.7%)	129.4(-0.6%)
	5.42	176.3(+0%)	130.2(+0%)
	1.14	150.8(-6.9%)	116.2(-7.1%)
4×4	2.16	154.3(-4.7%)	119.3(-4.6%)
	3.46	152.3(-5.9%)	118.2(-5.5%)
staggered	4.81	160.6(-0.8%)	124.3(-0.6%)
	5.62	161.9(+0%)	125.1(+0%)
	1.03	280.4(-7.0%)	138.2(-7.5%)
5×5	2.27	289.4(-3.9%)	139.2(-6.8%)
	3.12	291.3(-3.3%)	140.4(-6.1%)
staggered	3.89	300.5(-0.3%)	148.2(-0.9%)
	5.32	301.4(+0%)	149.5(+0%)
	1.03	501.6(-6.1%)	145.3(-7%)
6×6	2.34	449.1(-4.8%)	142.3(-8.9%)
in-line	3.19	459.2(-2.7%)	146.2(-6.4%)
in-iine	4.01	472.1(-0.1%)	155.9(-0.2%)
	5.18	472.9(+0%)	156.3(+0%)
	1.11	460.3(+7.2%)	142.2(-5.3%)
6×6	2.27	450.2(+4.8%)	143.8(-4.2%)
	3.09	415.3(-3.3%)	141.3(-5.9%)
staggered	4.58	428.5(-0.1%)	151.6(+0.9%)
	5.26	429.1(+0%)	150.2(+0%)
	1.36	600.2(+7%)	580.4(+6.8%)
straight	2.27	548.2(-1.6%)	530.6(-2.3%)
duct 5×5	3.16	550.2(-1.2%)	535.2(-1.4%)
staggered	4.19	559.4(-0.4%)	542.7(-0.7%)
Suggerou	5.13	557.1(+0%)	543.1(+0%)

bundle models in the bend duct were found to be 3.89 million, 4.60 million/4.81 million, and 4.01 million/4.58 million cells, respectively. The grid size for the staggered 5×5 tube-bundle model in the straight channel was determined to be 4.19 million cells. The results of the mesh sensitivity analysis are summarized in Table 3.

To validate the applicability of the RNG $k-\varepsilon$ turbulence model for the bend duct scenario, the results given by the RNG $k-\varepsilon$, standard $k-\varepsilon$, and $k-\omega$ shear-stress

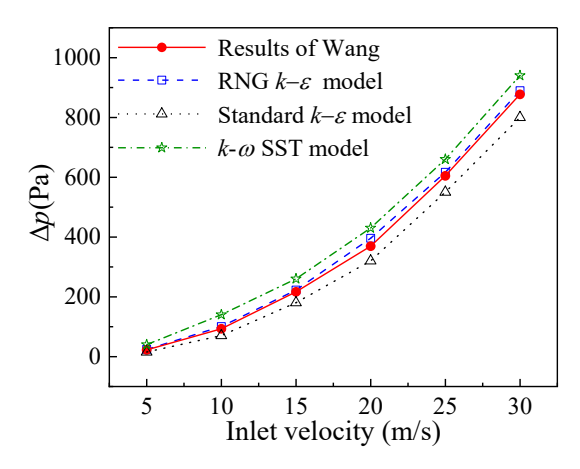


Fig. 6 Comparison of simulation results using different turbulence models with published results

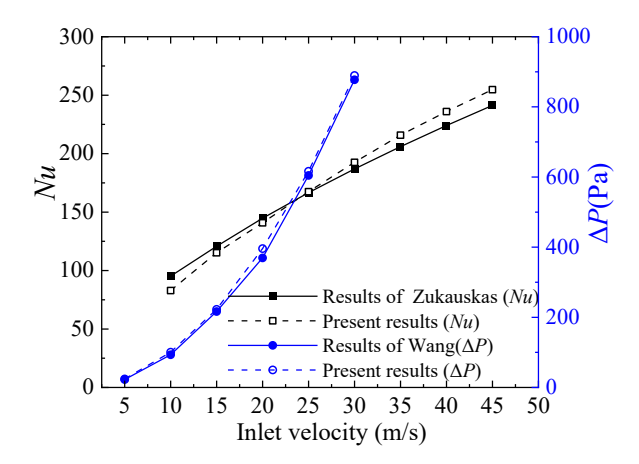


Fig. 7 Validation of simulated results with previous work

transport (SST) models were compared against simulation results (Wang et al., 2019). As shown in Fig. 6, the RNG $k-\varepsilon$ model shows better agreement with the reference data (Wang et al., 2019). Hence, this model was employed in the present study.

Figure 7 presents a comparison between the simulated values of Nu for gas flowing across a 5×5 in-line arrangement in the straight duct at various inlet velocities and the results calculated using Zukauskas' correlation (Zukauskas, 1986). As depicted in Fig. 7, there is a generally good agreement between the simulated and calculated values, with the maximum relative deviation of 13% observed at an inlet velocity of 10 m/s. For inlet velocities greater than 20 m/s, the relative deviation remains below 5%. The average relative deviation across all tested velocities is 5.2%.

Figure 7 also compares the simulated values of Δp in the bend duct without a tube-bundle heat exchanger with the results of Wang et al. (2019). The duct is similar to that in Fig. 1, with L_1 = 1400 mm, L_2 = 3600 mm, and H= 6600 mm. The inlet velocities were set to 5 m/s, 10 m/s, 15 m/s, 20 m/s, 25 m/s, and 30 m/s. Figure 7 shows that the simulated values obtained in this study deviate by a maximum of 7.6%, a minimum of 1.3%, and an average of 4.7% compared with the results reported by Wang et al. (2019). This validation demonstrates that the

computational method used in this study is reliable and that the simulation results are accurate.

3. RESULTS AND DISCUSSION

3.1 Effect of Tube-bundle Arrangement

3.1.1 Pressure Drop

Figure 8 illustrates the variation in Δp in 5×5 staggered and in-line tube-bundle arrangements placed in the bend duct as a function of Re, where $Re=u_{\rm max}d/v$, with d being the tube diameter (m), v the kinematic viscosity of air (m²/s), and $u_{\rm max}$ the average flow velocity at the minimum flow cross-section of the tube-bundle, given by $u_{\rm max} = (S_{\rm L}/d)u_0/(S_{\rm L}/d-1)$, where u_0 is the inlet velocity (m/s) and $S_{\rm L}$ is the longitudinal tube pitch (m).

As shown in Fig. 8, for the same Re, regardless of whether the tube bundle is arranged in a staggered or inline arrangement, Δp_b in the bend duct is always lower than $\Delta p_{\rm s}$ in the straight duct. Furthermore, for the in-line arrangement, $\Delta p_{\rm bi}$ is slightly lower than $\Delta p_{\rm si}$. For example, at $Re = 4.5 \times 10^4$, the pressure drop in the bend duct is 5.2% lower than that in the straight duct, while for the staggered arrangement, $\Delta p_{\rm bs}$ is noticeably lower than $\Delta p_{\rm ss}$, e.g., at Re = 4.5×10^4 , the pressure drop in the bend duct is 42.3%lower than that in the straight duct. The relationship of pressure drops in the four scenarios can be expressed as follows: $\Delta p_{ss} > \Delta p_{si} > \Delta p_{bi} > \Delta p_{bs}$, where the subscripts ss, si, bi, and bs denote the staggered arrangement in a straight duct, in-line arrangement in a straight duct, in-line arrangement in a bend duct, and the staggered arrangement in a bend duct, respectively. For the straight duct scenario, Δp_{si} for the in-line arrangement is significantly lower than that for the staggered arrangement $\Delta p_{\rm ss}$. For example, at $Re = 4.5 \times 10^4$, the pressure drop for the in-line arrangement is 34.5% lower than that for the staggered arrangement. For the bend duct, however, $\Delta p_{\rm bi}$ for the in-line arrangement is slightly higher than that for the staggered arrangement $\Delta p_{\rm bs}$. For example, at Re = 4.5 \times 10⁴, the pressure drop for the in-line arrangement is 7.2% higher than that for the staggered arrangement, which is clearly different from the straight duct scenario.

To investigate the underlying causes of the observed variations, Fig. 9 illustrates the streamline distribution at the z = 0.323 m cross-section for air flowing through staggered and in-line tube bundles in both bend and straight ducts at $Re = 2.5 \times 10^4$. For the staggered arrangement in the straight duct (Fig. 9(a)), based on Zdravkovich's definition of the wake characteristics behind horizontally placed twin cylindrical tubes (Zdravkovich, 1987), when the pitch ratio between the two tubes in the same horizontal plane is 4, the wake falls into the binary vortex street regime. In this regime, the shear layers that have detached from the upstream tube roll up into discrete vortices and are convected downstream in the staggered arrangement. However, due to the sufficiently large pitch, these vortices dissipate or reorganize before directly interacting with the downstream tube. As a result, the influence of the upstream wake on the downstream tube is significantly reduced, leading to a flow pattern in which the downstream tube behaves almost as if it were isolated. Consequently, the wake vortices generated by the

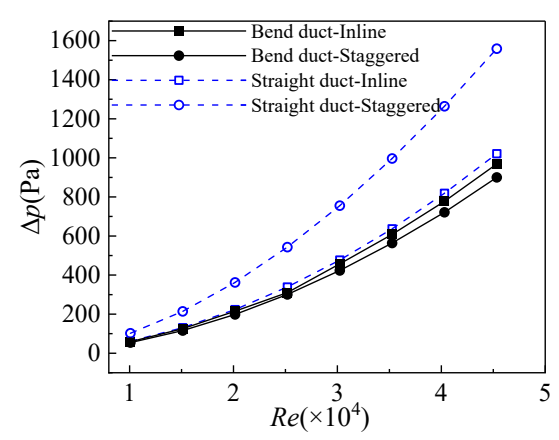


Fig. 8 Pressure drop of 5×5 in-line and staggered arrangements in the bend/straight duct as a function of *Re*

upstream tubes and their disturbances exert minimal influence on the downstream tube, resulting in similar hydrodynamic behaviors around each tube. Additionally, because the leading surface of the downstream tube is unaffected by the wake vortices from the upstream tube, the drag coefficients of the upstream and downstream tubes are nearly identical (Sadeghi et al., 2024). Furthermore, the continuously changing flow direction around the tube bundle leads to an increase in local flow resistance. This is due to frequent flow acceleration and deceleration between tube rows and enhanced turbulence generation at the junctions where flow paths contract and expand. These factors combine to contribute to the observed maximum Δp_{ss} in this scenario.

For the in-line arrangement in the straight duct (Fig. 9(b)), the pitch ratio of 2 places the wake behind the tubes within the reattachment regime (Zdravkovich, 1987). In this regime, the wake vortex shed by the upstream tube envelops the leading surface of the downstream tube. Closer examination reveals that the average velocity at the leading surface of the downstream tube is approximately 5 m/s. Additionally, an approximate stagnation vortex forms between the two tubes, allowing the majority of the fluid to pass directly through the free passage at the longitudinal pitch S_L to the downstream region, bypassing the other downstream tubes. This significantly reduces the vortex loss and, as a result, reduces the flow resistance around the downstream tube Δp_{si} (Feng. et al. 2013).

For the in-line arrangement in the bend duct (Fig. 9(c)), although the arrangement remains in-line, the hydrodynamic behaviors exhibit characteristics akin to a hybrid of an upper in-line arrangement and a lower staggered arrangement. In Region I, the hydrodynamic behaviors around the tubes resemble the in-line characteristics observed in Fig. 9(b), where the leading surface of the downstream tube is enveloped by the wake vortex of the upstream tube, generating a low-velocity zone on the downstream tube's leading surface. An approximate stagnation vortex forms between the two tubes, which contributes to a reduction in flow resistance in this region. In Region II, the hydrodynamic behaviors lie between the in-line and staggered arrangements, with the stagnation vortex decoupling into independent vortices. This leads to the emergence of a small high-speed zone on

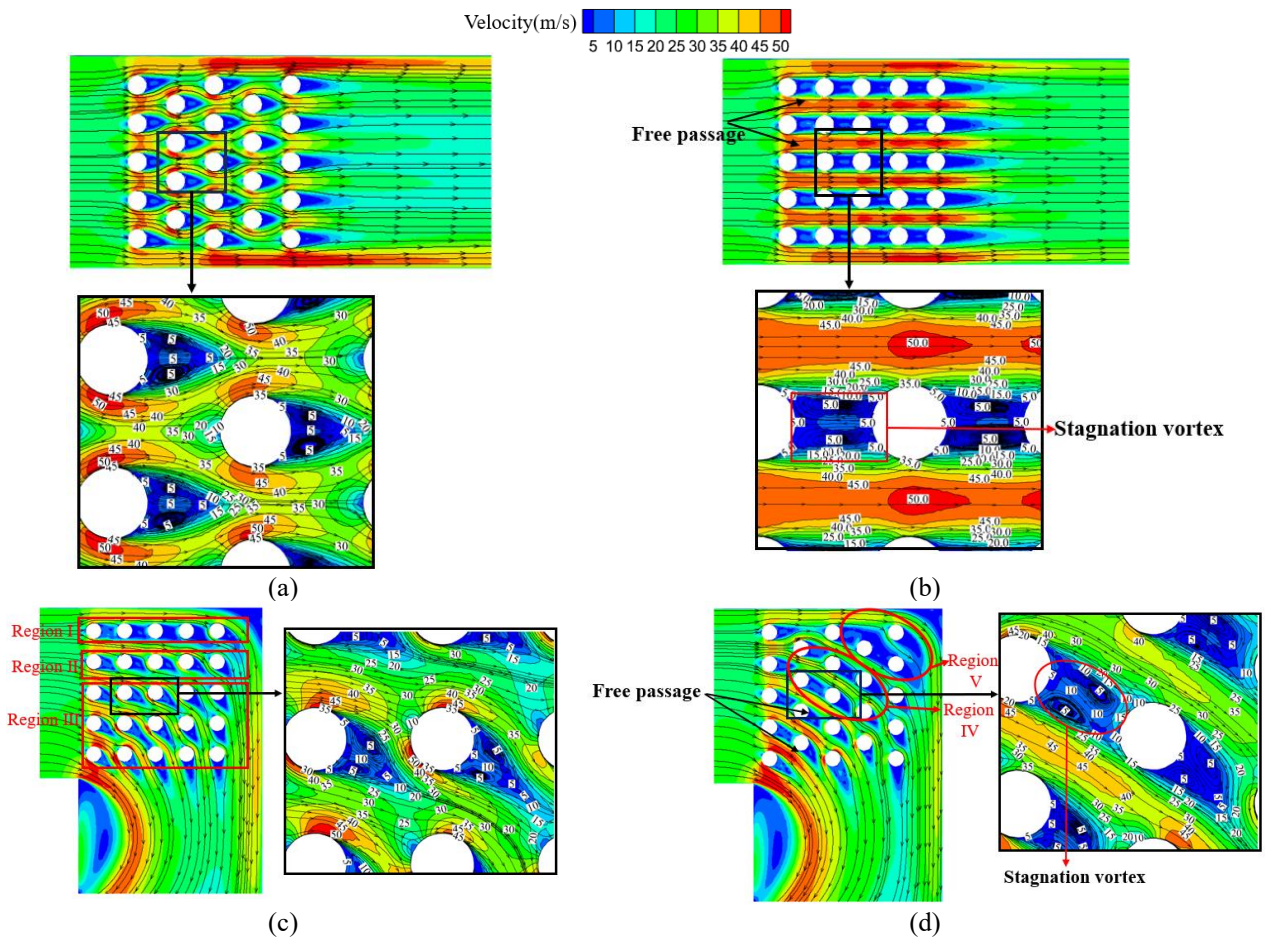


Fig. 9 Flow characteristics of 5×5 in-line and staggered arrangements in the bend and straight ducts at $Re=2.5\times10^4$. (a) staggered arrangement in the straight duct, (b) in-line arrangement in the straight duct, (c) in-line arrangement in the bend duct, and (d) staggered arrangement in the bend duct

the downstream tube's leading surface, while flows through the free passage remain evident in both Regions I and II. Near the tube-bundle exit, a portion of the fluid participates in the flow around individual tubes, although this still facilitates an overall reduction in flow resistance. In Region III, the hydrodynamic behaviors predominantly exhibit characteristics of the staggered arrangement, with some tubes continuing to be influenced by the wake vortex of the upstream tubes, resulting in a low-speed region on the downstream tube's leading surface. In contrast to Fig. 9(a), fewer tubes experience vortex-induced flow, particularly near the convex wall, where only 1–2 tubes are involved. This further diminishes flow resistance in this region. It is noteworthy that a substantial recirculation zone extends from the tube-bundle exit to the duct exit, resulting in an increase in the pressure drop in this region compared to the local pressure drop in the straight duct [See the results in Sec.3.1.1]. Considering these four factors, $\Delta p_{\rm bi}$ in this scenario is lower than $\Delta p_{\rm si}$ of the inline arrangement in the straight duct.

For the staggered arrangement in the bend duct (Fig. 9(d)), the hydrodynamic behaviors around the tube bundle exhibit characteristics that are broadly similar to those of the in-line arrangement. However, the flow turning and the increased pitch cause the approximate stagnation vortex to be confined to a localized region (Region IV). In Region V, two tubes are entirely enveloped by the wake vortex

from the upstream tube, resulting in a low-speed zone around their entire circumference, while the other vortices dissipate into independent single vortices, which influence the hydrodynamic behaviors on the leading surfaces of the downstream tubes. Despite this, free passages remain on both sides of the tubes in the streamwise direction. More significantly, the hydrodynamic patterns generated by the multiple tube-bundle function as deflectors, reducing drag. Compared with the in-line arrangement in Fig. 9(c), this scenario leads to a further reduction in the pressure drop. Additionally, the total number of tubes in this arrangement is 23, fewer than the 25 tubes in the in-line arrangement, which contributes to the lower local pressure drop. Taken together, these factors result in the smallest value of $\Delta p_{\rm bs}$ among the four scenarios.

3.1.2 Heat-transfer Rate

To compare the heat transfer performance under the four scenarios shown in Fig. 9, Figure 10 presents the heat-transfer rate per unit area when the air flows through 5×5 in-line and staggered tube bundles in the straight and bend ducts. The heat-transfer rate per unit area is $Q=Q_V/A$, where Q_t denotes the total heat transfer amount of the tube-bundle, given by $Q_t=cm\Delta t$, c is the specific heat capacity of air (kJ/(kg·K)), m is the mass flow rate of the inlet air (kg/s), Δt is the temperature difference between the inlet and outlet of the duct (K), A is the total surface area of the tube-bundle (m²).

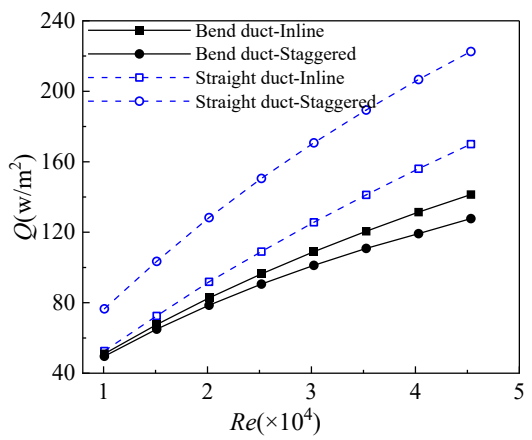


Fig. 10 Variation in heat transfer rate Q for 5×5 inline and staggered arrangements in the straight and bend ducts with Re

Figure 10 illustrates that, at the same Re, for both inline and staggered arrangements, Q_b in the bend duct is lower than Q_s in the straight duct. Specifically, for the inline arrangement, Q_{bi} is significantly lower than Q_{si} . At $Re = 4.5 \times 10^4$, the heat transfer rate in the bend duct is 16.8% lower than that in the straight duct. For the staggered arrangement, Q_{bs} is much lower than Q_{ss} . At $Re = 4.5 \times 10^4$,

the heat transfer rate in the bend duct is 42.6% lower than that in the straight duct. The heat-transfer rate per unit area in the four scenarios follows this order: $Q_{\rm ss} > Q_{\rm si} > Q_{\rm bi} > Q_{\rm bs}$. For the straight duct, $Q_{\rm si}$ for the in-line arrangement is notably lower than $Q_{\rm ss}$ for the staggered arrangement. At $Re = 4.5 \times 10^4$, the heat transfer rate for the in-line arrangement is 16.8% lower than that for the staggered arrangement. For the bend duct, however, $Q_{\rm bi}$ for the inline arrangement is higher than $Q_{\rm bs}$ for the staggered arrangement. At $Re = 4.5 \times 10^4$, the heat transfer rate for the in-line arrangement is 10.7% higher than that for the staggered arrangement, which is obviously different from the results in the straight duct.

To elucidate the fundamental mechanisms driving the observed variations, Fig. 11 illustrates the temperature distribution at the z=0.323 m cross-sectional plane for air flowing through both in-line and staggered tube-bundles in the straight and bend ducts under $Re=2.5\times10^4$. The staggered arrangement in the straight duct (Fig. 11(a)) induces continuous variations in the flow direction as it passes around each tube. This scenario generates enhanced flow disturbances and vortex shedding, which in turn reduce the thermal boundary layer thickness on the tube surfaces. Consequently, the thermal resistance between

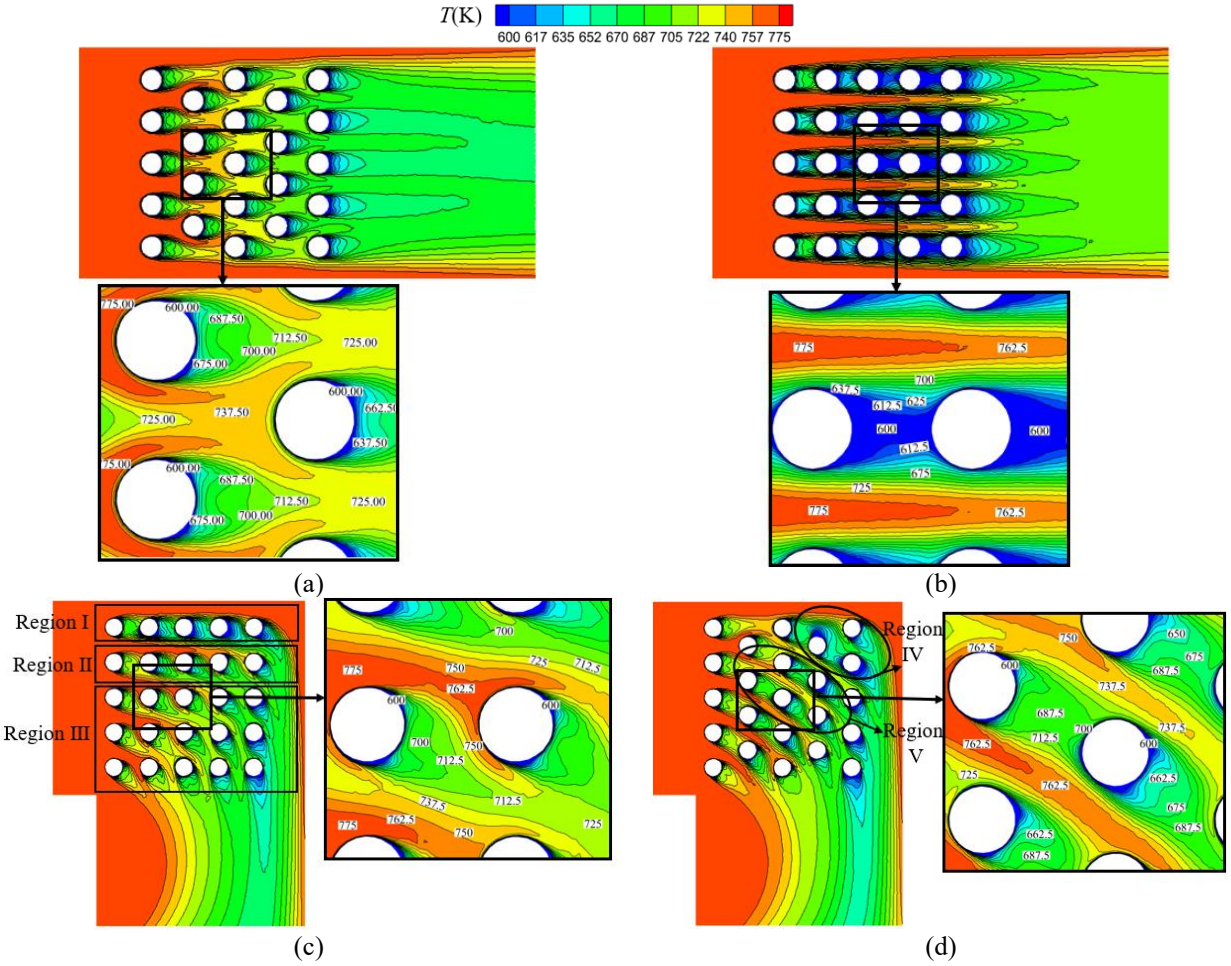


Fig. 11 Temperature distribution of 5×5 in-line and staggered arrangements in the straight and bend ducts at $Re = 2.5\times10^4$. (a) staggered arrangement in the straight duct, (b) in-line arrangement in the straight duct, (c) in-line arrangement in the bend duct, and (d) staggered arrangement in the bend duct

the tubes and the surrounding airflow is minimized, leading to improved heat transfer performance.

Furthermore, as the flow downstream of each tube enters the binary vortex street regime (Zdravkovich, 1987), the impact of the upstream tube's wake on the leading surface of the downstream tube is substantially diminished. A detailed examination of the locally enlarged view reveals that the leading surface of the downstream tube is predominantly exposed to higher-temperature fluids, and the increased temperature gradient between the fluid and the tube surface further augments the heat transfer of the tube bundle. These synergistic effects culminate in the most significant value of Q_{ss} occurring in this scenario.

For the in-line arrangement in the straight duct (Fig. 11(b)), the wake behind the upstream tube resides within the reattachment regime (Zdravkovich, 1987). This causes the wake region of the upstream tube to envelop the leading surface of the downstream tube, creating an approximate stagnant vortex between the two tubes. As a result, only a limited amount of high-temperature fluid can reach the leading surface of the downstream tubes, with the fluid temperature near the leading surface of the downstream tube being only 600 K. In contrast to the staggered arrangement shown in Fig. 11(a), this significantly reduces the temperature differential around the tube. Additionally, the stagnant vortex formation causes the majority of the high-temperature fluid to bypass the tube, flowing directly through the free passage to the downstream section, thereby minimizing the convective heat exchange with the tube surface. These factors lead to a considerable reduction in heat transfer efficiency, resulting in $Q_{\rm si}$ being significantly lower than $Q_{\rm ss}$ in the staggered arrangement.

For the in-line arrangement in the bend duct (Fig. 11(c)), the temperature distribution in Region I exhibits a pattern similar to that of the in-line arrangement in Fig. 11(b). The stagnant vortex between the upstream and downstream tubes attenuates the average temperature gradient around the tubes, which consequently diminishes the heat transfer capacity (Tsutsui, 2010). In Region II, the hydrodynamic behaviors surrounding the tube bundle transition from those of an in-line configuration to those observed in a staggered arrangement. The stagnant vortex undergoes a transformation into independent wake vortices, causing a portion of the leading surface of the downstream tube to be exposed to lower-temperature fluid. However, airflow through the free passage remains present in both Regions I and II. This permits a portion of the high-temperature fluid to bypass the tubes without engaging in significant heat exchange, further degrading the overall heat transfer in these regions. In Region III, although the flow behaviors around the tube bundle resemble those of the staggered arrangement, there are two critical differences when compared with the straight duct scenario. First, fewer tubes contribute hydrodynamic behavior than in the scenario shown in Fig. 11(a). Second, the change in flow direction leads to a shift in the position of the high-temperature fluid covering the leading surface of the downstream tube, moving from directly ahead (as in Fig. 11(a)) to the upper-left region of

the leading surface (Fig. 11(c)), as indicated by the red area. This spatial reconfiguration implies a change in the location of the highest local heat transfer coefficient around the tubes. Furthermore, in this region, the position of the highest local heat transfer coefficient varies from tube to tube. This contrasts with the straight duct scenario, in which the temperature distribution around each tube is relatively uniform. This localized variation in heat transfer results in an overall decrease in the average heat transfer performance. Taking all these factors into account, $Q_{\rm bi}$ in this scenario is lower than $Q_{\rm si}$ for the in-line arrangement in the straight duct.

For the staggered arrangement in the bend duct (Fig. 11(d)), the overall temperature distribution is similar to that of the in-line arrangement. However, the flow direction change and the increased pitch mean that the area in which the leading surface of the downstream tube is covered by lower-temperature fluid is confined to Region IV, while the tubes in Region V are mainly surrounded by low-temperature fluid. This reduces the temperature difference between the tubes and the surrounding fluid, thereby decreasing the heat transfer capacity. In other areas, part of the leading surface of the tubes is covered by lower-temperature fluid, with the fluid temperature slightly higher than in Regions IV and V. Additionally, from an overall perspective, the free passages are still present, and the high-temperature fluid passing through them flows out with little heat exchange. The above factors cause Q_{bs} in this scenario to be the lowest among the four configurations considered here.

3.1.3 PEC

Based on the above analysis, it can be concluded that for a tube-bundle heat exchanger arranged in the bend duct, although the $Q_{\rm bi}$ of the in-line arrangement is higher than the $Q_{\rm bs}$ of the staggered arrangement, $\Delta p_{\rm bi}$ of the in-line arrangement is also more significant than the $\Delta p_{\rm bs}$ of the staggered arrangement. To evaluate the overall performance of two impacts, a comprehensive performance evaluation index of PEC (Dogan, 2025; Kong et al., 2016) is used, expressed as follows:

$$PEC = \frac{Nu_{s} / Nu_{i}}{(f_{s} / f_{i})^{1/3}}$$
 (6)

where Nu_s and Nu_i denote the Nusselt numbers for staggered and in-line arrangements, respectively, and f_s and f_i denote the friction factors for staggered and in-line arrangements, respectively. The Nusselt number is defined as $Nu = hd/\lambda$, where h is the heat transfer coefficient (W/(m²-K)) and λ is the thermal conductivity of air (W/(m·K)). The friction factor is defined as $f = 2\Delta p/((L/D)\rho u^2_{max})$ (Kong et al., 2016), where $L = L_2 + L_4$, and ρ is the air density (kg/m³).

Figure 12(a) illustrates that, under different *Re* numbers, *PEC* remains consistently greater than 1. *PEC* serves as a key metric for assessing the balance between heat transfer enhancement and the associated increase in pressure drop. *PEC* values greater than 1 indicate that the overall thermal–hydraulic performance improvement is effective and beneficial, confirming that c the staggered

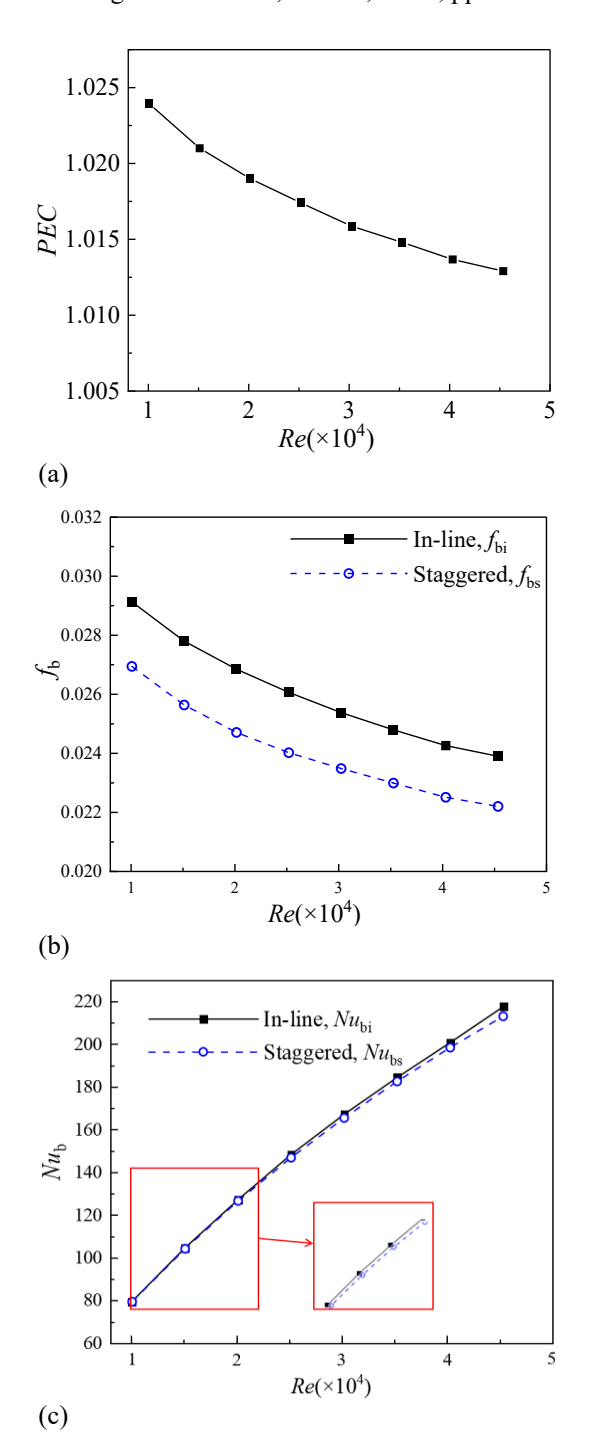


Fig. 12 Variations in PEC, Nu_b , and f_b with Re for 5×5 tube-bundle in the bend duct. (a) PEC, (b) f, and (c) Nu

arrangement in the bend duct achieves superior overall performance. Additionally, as Re increases, PEC exhibits a general decreasing trend. To elucidate the possible reasons, Figs. 12(b) and 12(c) depict the variations in f_b and Nu_b with Re. As shown in Fig. 12(b), both f_{bi} and f_{bs} decline with increasing Re, with f_{bi} maintaining a significantly higher magnitude than f_{bs} . Figure 12(c) indicates that Nu_{bi} is only slightly greater than Nu_{bs} . These findings suggest that the reduction in pressure drop achieved by the staggered arrangement in the bend duct has a dominant influence on PEC compared with the heat transfer enhancement observed in the in-line arrangement. Consequently, PEC remains consistently greater than 1.

As shown in Fig. 12(b), f_b gradually decreases with increasing Re. When Re increases from 1×10^4 to 4.5×10^4 , f_{bi} and f_{bs} decrease by 0.00523 and 0.00474, respectively, indicating that the increase in resistance loss for the in-line arrangement is higher than that for the staggered arrangement. The relative change rate, calculated as $(\Delta f_{bi} - \Delta f_{bs})/\Delta f_{bs}$, is 10.34%. Figure 12(c) shows that increasing Re from 1×10^4 to 4.5×10^4 causes Nu_{bi} and Nu_{bs} to increase by 136.14 and 133.87, respectively, with the relative change rate for the in-line arrangement, i.e., $(\Delta Nu_{bi} - \Delta Nu_{bs})/\Delta Nu_{bs}$, being only 1.69%. This indicates that resistance loss has a more significant impact on PEC, leading to a decrease in PEC as Re increases.

In summary, for the bend duct configurations, a holistic evaluation of both the thermal enhancement and flow resistance characteristics shows that staggered arrangements demonstrate superior overall thermohydraulic performance within the Re range of 1×10^4 to 4.5×10^4 . Furthermore, under the staggered scenario, comprehensive performance metrics exhibit more favorable outcomes at lower Re.

3.2 Effect of the Number of Tube Rows

Figures 13(a) and 13(b) illustrate the variations in f_b and Nu_b with Re for in-line and staggered tube-bundles arranged in 4×4, 5×5, and 6×6 configurations in the bend duct. Given a constant duct cross-sectional area, the characteristic velocity in the Re formulation is adopted with the inlet velocity u_0 , because $u_{\rm max}$ varies with the number of tube rows N.

Figure 13(a) demonstrates that, at a constant Re, f_b increases with N, which is consistent with the finding of Kwak et al. (2003). When N increases as we change from a 4×4 to a 5×5 configuration, f_b exhibits a marked increase. The average relative growth rate is 83.9% for the in-line arrangement and 82.5% for the staggered arrangement. However, as N increases further to the 6×6 configuration, the rate of increase in f_b diminishes, with relative growth rates of 35.8% for the in-line arrangement and 40.1% for the staggered arrangement. This behavior can be attributed to the reduction in tube pitch, as illustrated in Fig. 14 and Figs. 9(c)-9(d). As N increases, the tube pitch decreases, which results in a higher flow velocity between the tubes. This causes the high-speed regions behind the tubes to expand, thereby increasing the velocity gradient between the fluid and the tube, leading to a rise in frictional resistance. Furthermore, the decreased tube pitch induces increase in the vortex shedding frequency (Zdravkovich, 1987), contributing to an increase in local flow losses. The increase in N also raises the number of heat exchange tubes, thereby augmenting the flow resistance. Based on this analysis, it can be inferred that, for a given Re, f_b increases with N.

Under the same duct cross-section size and air flow rate, increasing N by moving from the 4×4 to the 5×5 configuration causes S_L and S_T to decrease from 100 mm and 100 mm to 80 mm and 80 mm, respectively; the pitch ratio (S_L/D) decreases from 2.5 to 2. When N increases further to a 6×6 configuration, S_L and S_T decrease to 70 mm and 70 mm, respectively, and the pitch ratio decreases

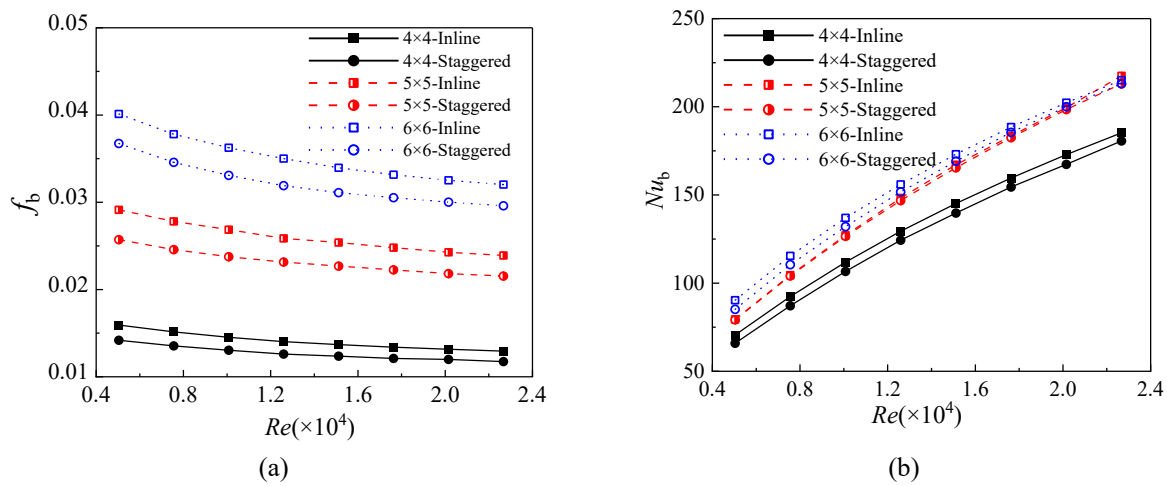


Fig. 13 Variations in f_b and Nu_b with Re for different tube row numbers in the bend duct. (a) variation in f_b and (b) variation in Nu

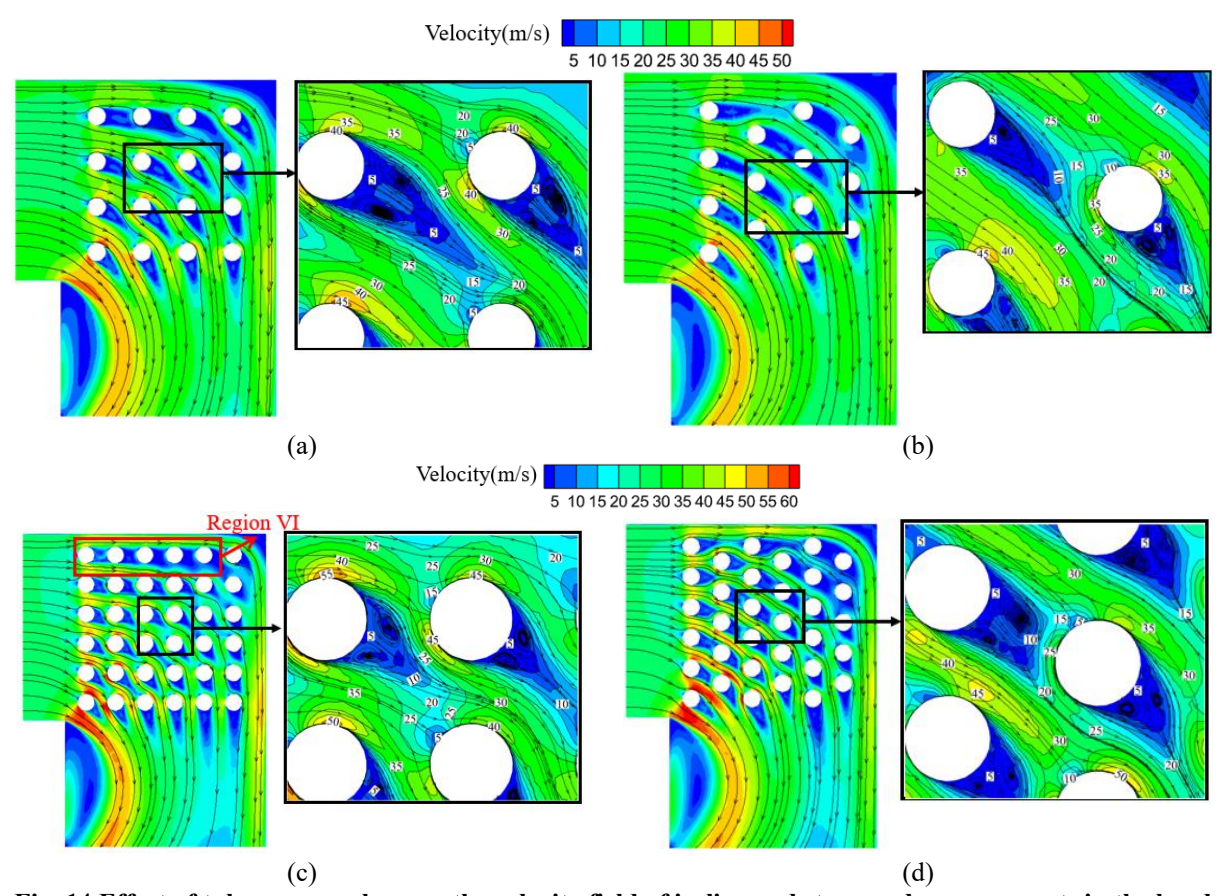


Fig. 14 Effect of tube row numbers on the velocity field of in-line and staggered arrangements in the bend duct ($Re = 2.5 \times 10^4$). (a) 4×4 in-line arrangement, (b) 4×4 staggered arrangement, (c) 6×6 in-line arrangement, and (d) 6×6 staggered arrangement

to 1.75. Namely, the change in the pitch ratio is smaller, thereby reducing the increase in the vortex shedding frequency (Zdravkovich, 1987). As depicted in Fig. 14 and Figs. 9(c)–9(d), the expansion of high-speed regions behind the tubes is significantly attenuated when transitioning from the 4×4 to the 6×6 configuration. The above factors contribute to a reduction in the increase of the local pressure drop (Kwak et al., 2003). Accordingly, as N increases from the 4×4 to the 5×5 configuration, f_b experiences a pronounced enhancement. However, with a further increase to the 6×6 configuration, the rate of

improvement becomes more gradual.

Figure 13(b) demonstrates that, at a constant Re, Nu_b exhibits an increasing trend with N, mirroring the behavior observed for f_b . A substantial increase in Nu_b occurs when N increases from the 4×4 to the 5×5 configuration. At $Re = 0.5 \times 10^4$, the relative growth rate is 12.5% for the inline arrangement and 17.4% for the staggered arrangement. At $Re = 2.3 \times 10^4$, the relative growth rate increases to 17.9% for the in-line and 20.3% for the staggered arrangement. However, as N is further increased to the 6×6

configuration, the rate of increase becomes marginal. At $Re = 0.5 \times 10^4$, the relative growth rate is 10.7% for the inline arrangement and 7.4% for the staggered arrangement. For $Re > 1.25 \times 10^4$, Nu_b is almost identical for the 5×5 and 6×6 configurations. These behaviors can be primarily attributed to the decrease in tube pitch as N increases, which narrows the inter-tube spacing and consequently accelerates the local flow velocity. This increase in velocity enhances both the turbulence intensity and the convective heat transfer rate between the fluid and the tubes. Taking the in-line arrangement as an example, for the 4×4 configuration, Fig. 15(a) shows that the leading surface of the tube bundle in the third row and the third column is surrounded by fluid at 760 K for heat exchange. In the 5×5 configuration, as depicted in Fig. 11(c), the leading surface of the tube-bundle in the third row and third column is exposed to fluid at 763 K, whereas for the 6×6 configuration (Fig. 15(c)), the leading surface of the tube-bundle in the third row and third column is surrounded by fluid at 766 K. These observations suggest that the increase in temperature difference further augments the heat exchange efficiency. Moreover, the total number of heat exchange tubes increases with N, as evidenced by Fig. 15, which shows a significant reduction in the amount of high-temperature air exiting the duct without adequate heat exchange. Considering the above factors, it can be inferred that, for a constant Re, Nub increases with the number of tube rows.

When N increases from the 4×4 to the 5×5 and 6×6 configurations, the pitch ratio decreases from 2.5 to 2 and 1.75, respectively. When moving to the 6×6 configuration, the reduction in the pitch ratio is less pronounced, and so

the increase in local flow velocity is also reduced, leading to a smaller enhancement in the convective heat transfer between the fluid and the tubes. Additionally, in the 6×6 configuration, as shown in Region VI in Fig. 14(c), both the upstream and downstream tubes are in the single slender body regime. As the free shear layer from the upstream tube bypasses the downstream tubes, the degree of mixing between fluid particles inside and outside the single slender body regime is reduced. As a result, the gas temperature within the approximate stagnant vortices decreases, leading to a reduction in heat transfer efficiency, as previously reported (Ahmadi, 2024). Thus, although the number of heat exchange tubes increases more significantly when N increases from the 4×4 to the 5×5 configuration compared with the 6×6 configuration, the rate of increase in Nu is reduced in the 6×6 configuration due to the factors discussed above. At high Re, the thermal boundary layer on the tube surface becomes relatively thin, and there is no further potential for heat transfer enhancement. Moreover, at high Re, the increased inertial forces make the flow more prone to instability, resulting in greater energy losses. This prevents the flow from overcoming the adverse pressure gradient at the front of the tube, causing the separation point of the free shear layer to move upstream (Zhou et al., 2009). Under the influence of inertial forces, the fluid tends to move along its original direction, increasing the width of the wake region, i.e., the low-speed zone. This diminishes the area of the high-temperature fluid that is in contact with the heat transfer surface, thereby decreasing the efficient heat transfer area. Therefore, when $Re > 1.25 \times 10^4$, the Nu values for the 6×6 and 5×5 configurations are almost identical.

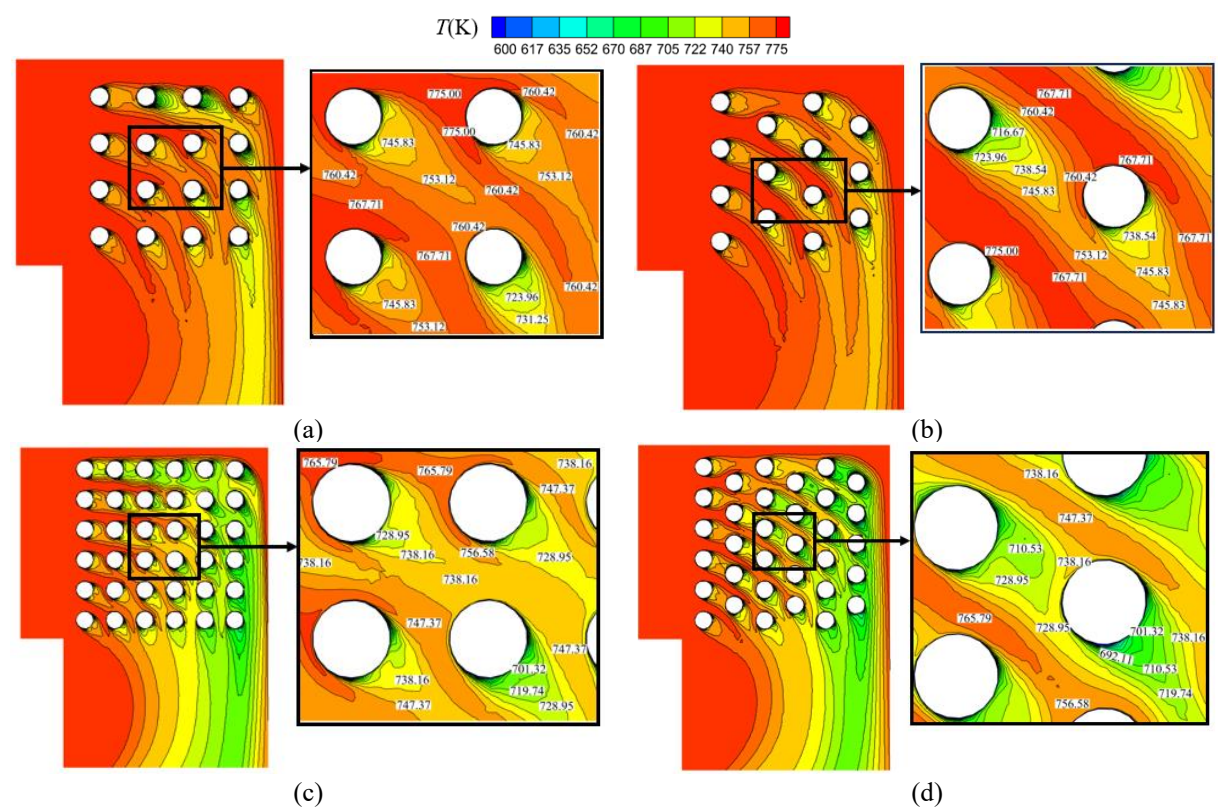


Fig. 15 Effect of tube row numbers on the temperature distribution of in-line and staggered arrangements in the bend duct ($Re = 2.5 \times 10^4$). (a) 4×4 in-line arrangement, (b) 4×4 staggered arrangement, (c) 6×6 inline arrangement, and (d) 6×6 staggered arrangement

3.3 Empirical Formula Correction

The above analysis underscores that the hydrodynamics and heat transfer performance of tube-bundle heat exchangers in bend ducts exhibit significant differences compared with those in straight ducts. The applicability of empirical formulas developed for straight ducts to the case of bend ducts, as well as the impact of N and the tube arrangement, necessitates further comprehensive investigation.

3.3.1 Pressure Drop Formula Correction

For a tube bundle arranged in the straight duct, Holman (2002) recommends using Jakob's (Jakob, 1938) empirical formula to determine the air-side pressure drop for a crossflow passing tube bundle, given as follows:

$$\Delta p = \frac{2fG_{\text{max}}^2 N}{\rho} \left(\frac{\mu_{\text{w}}}{\mu_{\text{b}}}\right)^{0.14} \tag{7}$$

where G_{max} is the mass flow rate (kg/m²·s) corresponding to the average flow velocity at the smallest flow cross-section of the tube bundle, N is the number of tube rows, ρ is the air density (kg/m³), μ_{w} is the air dynamic viscosity (Pa·s) determined at the tube wall temperature, and μ_{b} is the dynamic viscosity (Pa·s) at the average inlet and outlet air temperature. The friction factor for an in-line arrangement is given by

$$f_{\rm si} = \left\{ 0.044 + \frac{0.08S_{\rm T} / d}{\left[(S_{\rm L} - d) / d \right]^{0.43 + 1.13d / S_{\rm T}}} \right\} Re^{-0.15}$$
 (8)

That for a staggered arrangement, given by

$$f_{ss} = \left\{ 0.25 + \frac{0.118}{\left[\left(S_{L} - d \right) / d \right]^{1.08}} \right\} Re^{-0.16}$$
 (9)

Figure 16 compares the pressure drop values $\Delta p_{\rm b,m}$ obtained from the present simulations with the results for $\Delta p_{\rm s,e}$ calculated from Eq. (7); here, the subscripts m and e denote the present modeling and empirical formulas, respectively. There is a significant deviation between the two results, particularly for the staggered arrangement. Taking $\Delta p_{\rm s,e}$ as the reference, within the Re range considered in this study, the staggered arrangement produces average relative deviations of $(\Delta p_{\rm ss,e} - \Delta p_{\rm bs,m})/\Delta p_{\rm ss,e} = 55.8\%$, 48.8%, and 57.5% for the 4×4, 5×5, and 6×6 tube arrangements, respectively. For the in-line arrangement, the average relative deviations are $(\Delta p_{\rm si,e} - \Delta p_{\rm si,e})$

 $\Delta p_{\rm bi,m}/\Delta p_{\rm si,e} = 26.3\%$, 16.3%, and 28.6%. As indicated in Section 3.2, the main reason for these deviations is the significant difference in the flow patterns between the straight and bend ducts. Such deviations, if not corrected, could result in significant deviations in practical heat exchanger design. Therefore, it is necessary to make appropriate corrections to the friction factor f in Eqs. (8) and (9) to determine the pressure drop in the bend duct accurately.

Equations (10) and (11) indicate the coefficients to be modified. The coefficients A and A' can be regarded as flow losses passing the duct, while the following term accounts for the local losses induced by the tube bundle. Before correcting Eqs. (8) and (9), the pressure drop of the duct without a tube bundle is simulated to assess the impact of the duct geometry on the flow losses. The geometric model is shown in Fig. 17; the specific parameters are provided in Section 2.

$$f_{bi} = \left\{ A + \frac{BS_{T} / d}{\left[(S_{L} - d) / d \right]^{C + Dd / S_{T}}} \right\} Re^{-0.15}$$
 (10)

$$f_{bs} = \left\{ A' + \frac{B'}{\left[(S_1 - d) / d \right]^{C'}} \right\} Re^{-0.16}$$
 (11)

For $Re = 1 \times 10^4$, with u_0 serving as the characteristic velocity, the pressure drop in the straight duct is 8.2 Pa, whereas that in the bend duct increases significantly to 34.2 Pa. This disparity arises because the pressure drop in the straight duct is primarily attributed to viscous frictional losses, while in the bend duct, the pressure drop is influenced by viscous frictional losses and additional losses associated with the bend, which are considerably higher than the frictional losses. Therefore, when adjusting the correction coefficients in Eqs. (10) and (11), the values of A and A' must be constrained to exceed the uncorrected coefficients of 0.044 and 0.25, respectively, which are valid for the straight duct.

This study employs nonlinear regression analysis based on the least-squares approach, with Python's SciPy optimization module used to achieve systematic identification of multiparameter-coupled equation systems, thereby obtaining the necessary coefficients. The coefficients in Eqs. (10) and (11) for both arrangement types are listed in Table 4. A comparison between the corrected $\Delta p_{\rm b,e}$ and the simulated $\Delta p_{\rm b,m}$, and the average

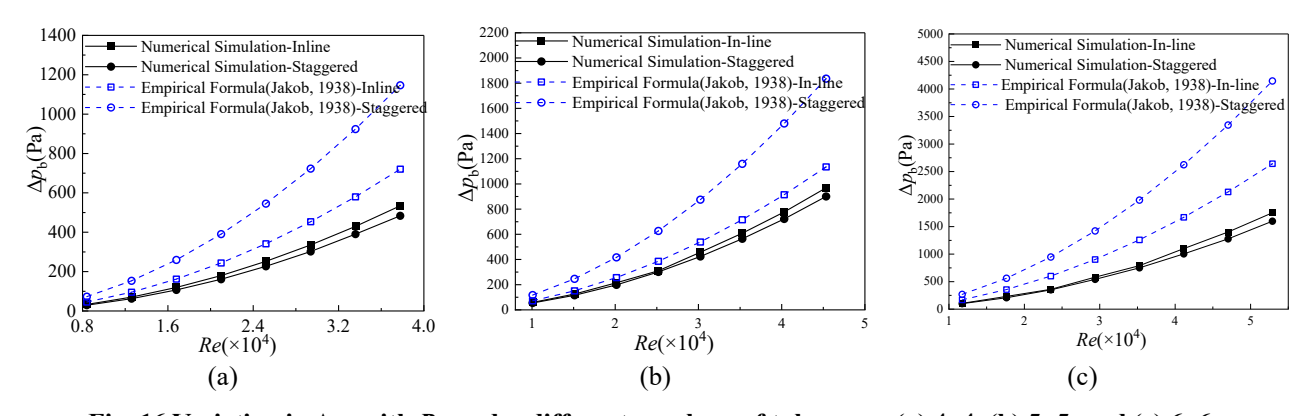


Fig. 16 Variation in Δp_b with Re under different numbers of tube rows. (a) 4×4 , (b) 5×5 , and (c) 6×6

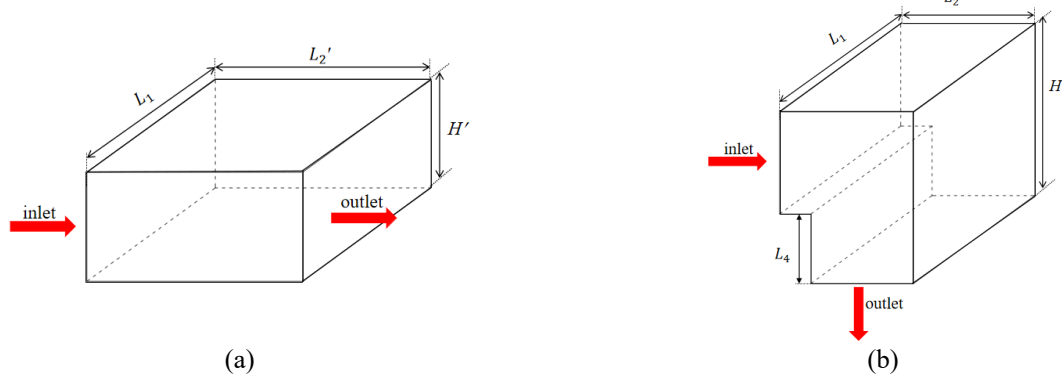


Fig. 17 Schematic diagram of the duct model without a tube-bundle. (a) straight duct, and (b) bend duct

Table 4 Coefficient correction in the friction factor f

Tube arrange ments	Friction factor f	Undeter mined coeffici ents	Befor e corre ction	After corre ction
In-line	$f_{bi} = \left\{ \mathbf{A} + \frac{\mathbf{B}S_{\mathrm{T}} / d}{\left[(S_{\mathrm{L}} - d) / d \right]^{\mathrm{c}}} \right\}$	$\frac{A}{\underset{t+\mathrm{D}d/S_{\mathrm{T}}}{B}Re^{-0.}}$	0.044 5 0.080 0.430 1.130	0.082 0.024 0.187 0.140
Stagger ed	$f_{bs} = \left\{ \mathbf{A}' + \frac{\mathbf{B}'}{\left[(S_{L} - d) / d \right]} \right\}$	A' E' $RE^{0.16}$ C'	0.250 0.118 1.080	0.277 - 0.145 0.100

Table 5 Comparison of average deviation between the simulated and calculated results using empirical formulas

Tube arrangemen ts	Numb er of tube rows	Average deviation before correction (%) $(\Delta p_{s,e} - \Delta p_{b,m})/\Delta$ $p_{s,e}$	Average deviation after correction (%) $(\Delta p_{\text{b,e}} - \Delta p_{\text{b,m}})/\Delta$ $p_{\text{b,e}}$
	4×4	26.3	0.6
In-line	5×5	16.3	5.0
	6×6	28.6	3.6
Staggered	4×4	55.8	2.1
	5×5	48.8	6.8
	6×6	57.5	2.3

relative deviation, i.e., $(\Delta p_{b,e} - \Delta p_{b,m})/\Delta p_{b,e}$, is presented in Table 5. The corrected results are highly consistent with the simulated results, with a maximum relative deviation of 6.51%, which is much lower than that prior to correction. Therefore, the corrected friction factor formulas are suitable for determining the pressure drop in the tube-bundle heat exchanger in the bend duct.

For the in-line arrangement,

$$f_{\rm bi} = \left\{ 0.082 + \frac{0.024 S_{\rm T} / d}{\left[(S_{\rm L} - d) / d \right]^{0.187 + 0.14d / S_{\rm T}}} \right\} Re^{-0.15}$$
 (12)

For the staggered arrangement,

$$f_{\rm bs} = \left\{ 0.277 - \frac{0.145}{\left[(S_{\rm L} - d) / d \right]^{0.1}} \right\} Re^{-0.16}$$
 (13)

3.3.2 Nu Formula Correction

The Zukauskas empirical correlation (Zukauskas, 1986) is commonly used to determine the surface heat transfer coefficient for heat exchangers in straight ducts. For an air crossflow over an in-line tube bundle in the Re range of 10^3 to 2×10^5 , Nu is given by,

$$Nu_{\rm si} = \varepsilon_{\rm n} 0.27 Re^{0.63} Pr_{\rm f}^{0.36} \left(\frac{Pr_{\rm f}}{Pr_{\rm w}}\right)^{0.25}$$
 (14)

For an air crossflow over a staggered tube bundle,

$$Nu_{\rm ss} = \varepsilon_{\rm n} \, 0.35 \left(\frac{S_{\rm L}}{S_{\rm T}} \right)^{0.2} Re^{0.6} Pr_{\rm f}^{0.36} \left(\frac{Pr_{\rm f}}{Pr_{\rm w}} \right)^{0.25}$$
 (15)

where ε_n is the correction factor for N, Pr_f is the Prandtl number at the reference temperature (i.e., the average temperature of the fluid at the inlet and outlet of the tube bundle), and Pr_w is the Prandtl number determined at the tube wall temperature.

Figure 18 compares the simulated values $Nu_{b,m}$ with the calculated values $Nu_{\rm si,e}$ and $Nu_{\rm ss,e}$ from Eqs. (14) and (15). There is a significant deviation between $Nu_{b,m}$ and $Nu_{s,e}$. Taking $Nu_{s,e}$ as the reference, for the staggered arrangement, the average relative deviations are $(Nu_{ss,e} Nu_{\rm bs,m}$)/ $Nu_{\rm ss,e}$ = 16.1%, 18.7%, and 10.2% for the 4×4, 5×5, and 6×6 tube arrangements, respectively; for the in-line arrangement, the average relative deviations are $(Nu_{\rm si,e} Nu_{bi,m}$ / $Nu_{si,e}$ = 15.2%, 12.8%, and 8.9%. As previously analyzed, the main reason for the above deviations is the change in flow patterns in the bend duct. Therefore, it is necessary to modify the coefficients in Eqs. (14) and (15). Close inspection of Eqs. (14) and (15) shows that the exponents of Pr_f and Pr_f/Pr_w are the same for both arrangements. This suggests that these exponents are relatively insensitive to the tube arrangement, and their influence on the deviation is likely secondary compared to the overall geometric and flow field alterations introduced by the bend geometry. Thus, the influence of the tube arrangement on these exponents can be neglected, i.e., the exponents require no modification. Additionally, in the geometry considered in this study, $S_L = S_T$, and so the coefficient of S_L/S_T in Eq. (15) remains unaltered Eqs. (16) and (17) indicate that the coefficients need to be corrected. By employing the same parameter fitting methodology as presented in the previous subsection, the corrected

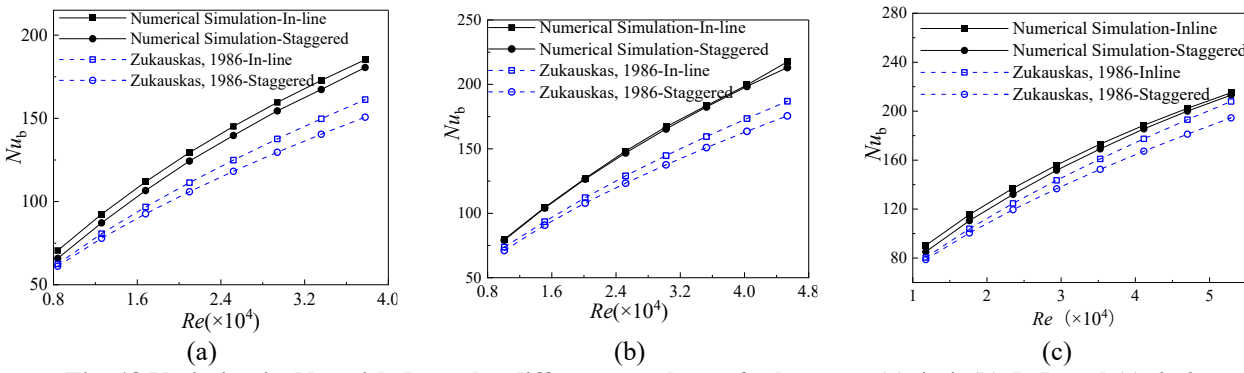


Fig. 18 Variation in Nu_b with Re under different numbers of tube rows. (a) 4×4 , (b) 5×5 , and (c) 6×6

		-		
Tube	Nu Formulas	Undetermined	Before	After
arrangements	Nu Formulas	coefficients	correction	correction
In-line	$Nu_{\rm bi} = \varepsilon_{\rm n} a R e^{\rm b} P r_{\rm f}^{0.36} \left(\frac{P r_{\rm f}}{P r_{\rm w}} \right)^{0.25}$	a	0.27	0.50
III IIIIC		ь	0.63	0.58
Staggered	$Nu_{\rm bs} = \varepsilon_{\rm n} a' \left(\frac{S_{\rm L}}{S}\right)^{0.2} Re^{\rm b'} Pr_{\rm f}^{0.36} \left(\frac{Pr_{\rm f}}{Pr}\right)^{0.25}$	a'	0.35	0.44
		b.'	0.60	0.50

Table 6 Coefficient correction in the Nu empirical formulas

Table 7 Comparison of average deviation between the simulated and calculated results using empirical formulas.

Tube arrangemen ts	Tub e row s	Average deviation before correction (%) (Nu _{s,e} -Nu _{b,m})/Nu _{s,e}	Average deviation after correction (%) (Nu _{b,e} -Nu _{b,m})/Nu _{b,e}
	4×4	15.2	3.6
In-line	5×5	12.8	3.8
	6×6	8.9	2.5
Staggered	4×4	16.1	4.1
	5×5	18.7	5.7
	6×6	10.2	2.8

coefficients for both arrangements were calculated. The results are listed in Table 6. The average relative deviations between the corrected values $Nu_{\rm b,e}$ and the simulated values $Nu_{\rm b,m}$, i.e., $(Nu_{\rm b,e}-Nu_{\rm b,m})/Nu_{\rm b,e}$, are listed in Table 7.

$$Nu_{\rm bi} = \varepsilon_{\rm n} a R e^{\rm b} P r_{\rm f}^{0.36} \left(\frac{P r_{\rm f}}{P r_{\rm w}} \right)^{0.25}$$
 (16)

$$Nu_{\rm bs} = \varepsilon_{\rm n} a' \left(\frac{S_{\rm L}}{S_{\rm T}}\right)^{0.2} Re^{\rm b'} Pr_{\rm f}^{0.36} \left(\frac{Pr_{\rm f}}{Pr_{\rm w}}\right)^{0.25}$$
 (17)

The results in Table 7 indicate that, compared with the results prior to correction, the relative deviation is significantly decreased, greatly improving the accuracy of the prediction results. Therefore, the corrected formulas are suitable for the prediction of Nu_b for heat exchangers in bend ducts under the conditions explored in this study.

For the in-line arrangement,

$$Nu_{\rm bi} = \varepsilon_{\rm n} \, 0.5 Re^{0.58} Pr_{\rm f}^{0.36} \left(\frac{Pr_{\rm f}}{Pr_{\rm w}} \right)^{0.25}$$
 (18)

For the staggered arrangement,

$$Nu_{\rm bs} = \varepsilon_{\rm n} \, 0.44 \left(\frac{S_{\rm L}}{S_{\rm T}} \right)^{0.2} Re^{0.59} Pr_{\rm f}^{0.36} \left(\frac{Pr_{\rm f}}{Pr_{\rm w}} \right)^{0.25}$$
 (19)

4. CONCLUSION

The hydrodynamics and heat transfer performance of tube-bundle heat exchangers arranged in rectangularsection right-angle bend ducts differ significantly from those in straight ducts due to the distinct hydrodynamic behaviors in the bend duct. In straight ducts with a staggered arrangement, the wake vortices behind the upstream tubes have minimal impact on the downstream tubes, resulting in similar hydrodynamic behaviors across all tubes. In straight ducts with an in-line arrangement, the leading surface of the downstream tube is influenced by the wake vortex from the upstream tube, forming an approximate stagnant vortex between the two tubes. The hydrodynamic behaviors in this configuration resemble those of a mixed arrangement, consisting of an upper inline arrangement and lower staggered arrangement. In the staggered arrangement of the bend duct, the hydrodynamic behaviors are akin to those of a crossflow in-line tube bundle, although there are regions where lowspeed fluid surrounds the entire circumference of the tubes. Additionally, the number of tubes in this configuration is smaller than that in the in-line arrangement.

From this, the relationship between the pressure drops in four scenarios was determined to be $\Delta p_{\rm ss} > \Delta p_{\rm si} > \Delta p_{\rm bi} > \Delta p_{\rm bs}$, and the relationship for heat transfer rate was found to be $Q_{\rm ss} > Q_{\rm si} > Q_{\rm bi} > Q_{\rm bs}$. Because the pressure drop reduction effect for the staggered arrangement is higher than the enhanced heat transfer effect for the in-line arrangement, the comprehensive *PEC* for the staggered arrangement in the bend duct was observed to be higher than that for the in-line arrangement.

In the bend duct, as the number of tube rows increases,

both f_b and Nu_b increase, but the increase is influenced by the reduction in tube pitch. When N increases from the 4×4 to the 5×5 configuration, both f_b and Nu_b increase significantly; however, when N increases from the 5×5 to the 6×6 configuration, the increase in f_b and Nu_b diminishes. Furthermore, for $Re > 1.25 \times 10^4$, the values of Nu_b for the 5×5 and 6×6 configurations are nearly identical.

By correcting $\Delta p_{\rm s}$ and $Nu_{\rm s}$ for straight ducts, this study has derived superior empirical correlations for predicting both $\Delta p_{\rm b}$ and $Nu_{\rm b}$ in bend ducts, which are specifically developed for inlet Re values ranging from 1×10^4 to 4.5×10^4 and for tube pitch-to-diameter ratios of S/D = 1.75, 2, and 2.5.

$$\begin{aligned} Nu_{\rm bi} &= \varepsilon_{\rm n} \, 0.5 R e^{0.58} P r_{\rm f}^{0.36} \left(\frac{P r_{\rm f}}{P r_{\rm w}} \right)^{0.25} \\ Nu_{\rm bs} &= \varepsilon_{\rm n} \, 0.44 \left(\frac{S_{\rm L}}{S_{\rm T}} \right)^{0.2} R e^{0.59} P r_{\rm f}^{0.36} \left(\frac{P r_{\rm f}}{P r_{\rm w}} \right)^{0.25} \\ f_{\rm bi} &= \left\{ 0.082 + \frac{0.024 S_{\rm T} \, / \, d}{\left[(S_{\rm L} - d) \, / \, d \right]^{0.187 + 0.14 d / S_{\rm T}}} \right\} R e^{-0.15} \\ f_{\rm bs} &= \left\{ 0.277 - \frac{0.145}{\left[(S_{\rm L} - d) \, / \, d \right]^{0.1}} \right\} R e^{-0.16} \end{aligned}$$

The values calculated using the corrected formulas match the simulated values well, significantly improving the prediction accuracy and providing a theoretical basis for the design and optimization of this type of heat exchanger.

CONFLICT OF INTEREST

The authors have no conflicts to disclose.

AUTHORS CONTRIBUTION

Xin Wang: Formal analysis (equal); Software; Writing—original draft (equal). **Chunxi Li**: Supervision (equal); Writing — review & editing (equal). **Yaru Yan**: Investigation (equal); Data curation (equal). **Xuemin Ye**: Conceptualization (equal); Methodology (equal); Formal analysis (equal).

REFERENCES

- Ahmadi, N. (2024). Influences of optimizing the turbulator arrangement on the heat transfer and hydraulic characteristics of the tubular heat exchanger. *International Journal of Thermal Sciences*, 197, 108792. https://doi.org/10.1016/j.ijthermalsci.2023.108792
- Batista, J., Trp, A., Lenic, K., & Kirincic, M. (2025). The influence of geometry parameters of rectangular vortex generators on the air-to-water fin-and-tube heat exchanger efficiency enhancement. *International Communications in Heat and Mass Transfer*, 162, 108647. https://doi.org/https://doi.org/10.1016/j.icheatmasstr

ansfer.2025.108647

- Bennour, E., Kezrane, C., Kaid, N., Alkhafaji, M., Alhassan, M., & Menni, Y. (2024). Numerical Assessment of Vortex Generators for Enhancing Thermal Performance in Corrugated Tubes. *Journal of Applied Fluid Mechanics*, *17*(10), 2115-2127. https://doi.org/10.47176/jafm.17.10.2460
- Che, M., & Elbel, S. (2021). Experimental quantification of air-side row-by-row heat transfer coefficients on fin-and-tube heat exchangers. *International Journal of Refrigeration*, 131, 657-665. https://doi.org/10.1016/j.ijrefrig.2021.06.012
- Córcoles, J., Díaz-Heras, M., Coy, P. D., & Almendros-Ib áñez, J. (2024). 3-D numerical simulation of the heat transfer of a fluidized bed with a horizontal tube bundle and Geldart D particles. *International Journal of Heat and Mass Transfer*, 225, 125406. https://doi.org/10.1016/j.ijheatmasstransfer.2024.12
- Deeb, R. (2023). Enhancing heat exchanger performance through hybrid angle of attack control for drop-shaped tubes. *Physics of Fluids*, *35*(8), 085122. https://doi.org/10.1063/5.0160385
- Derakhshandeh, J., & Alam, M. M. (2019). A review of bluff body wakes. *Ocean Engineering*, *182*, 475-488. https://doi.org/10.1016/j.oceaneng.2019.04.093
- Dogan, S. (2025). Baffle angle optimization of a typical shell and tube heat exchanger. *Physics of Fluids*, 37(1), 015165. https://doi.org/10.1063/5.0249271
- Feng, Z., Zhang, Y., & Zang, F. (2013). Numerical simulation of flow-induced vibration in straight tube bundles. *Applied Mathematics and Mechanics*, 34(11), 1165-1172. https://doi.org/10.11949/0438-1157.20190527
- Holman, J. P. (2002). *Heat Transfer*. Tata McGraw-Hill Education.
- Hu, S., Zhu, L., Zhang, M., Tang, X., & Wang, X. (2023). Development and prospect of vacuum high-pressure gas quenching technology. *Materials*, *16*(23), 7413. https://doi.org/10.3390/ma16237413
- Jakob, M. (1938). Discussion: Heat transfer and flow resistance in cross flow of gases over tube banks. *Transactions of the American Society of Mechanical Engineers*, 60(4), 384-386. https://doi.org/10.1115/1.4020766
- Karabulut, K. (2024). The effects of rectangular baffle angles and heights on heat transfer and pressure drop performance in cross-triangular grooved rectangular flow ducts. *International Journal of Heat and Fluid Flow*, 105, 109260. https://doi.org/https://doi.org/10.1016/j.ijheatfluidflow.2023.109260
- Kong, Y., Yang, L., Du, X., & Yang, Y. (2016). Effects of continuous and alternant rectangular slots on thermoflow performances of plain finned tube bundles in inline and staggered configurations. *International*

- Journal of Heat and Mass Transfer, 93, 97-107. https://doi.org/10.1016/j.ijheatmasstransfer.2015.10. 008
- Kwak, K., Torii, K., & Nishino, K. (2003). Heat transfer and pressure loss penalty for the number of tube rows of staggered finned-tube bundles with a single transverse row of winglets. *International Journal of Heat and Mass Transfer*, 46(1), 175-180. https://doi.org/10.1016/S0017-9310(02)00235-1
- Lang, C., Lu, C., Sun, B., Xin, C., Zhou, T., & Fu, T. (2024). Performance comparison of inline and staggered integrally-molded spiral finned tubes for low-carbon emissions. *Applied Thermal Engineering*, 241, 122355. https://doi.org/10.1016/j.applthermaleng.2024.1223
- Liu, C., Jia, L., Dang, C., Cui, Z., & Yin, L. (2021). Effect of Liquid-Vapor Separation on the Thermal-Hydraulic Performance of an Air-Cooled Condenser. *Journal of Enhanced Heat Transfer*, 28(3), 63-90. https://doi.org/10.1615/JEnhHeatTransf.202103637
- Moharana, S., Sha, B. B., Das, M. K., Pecherkin, N. I., Pavlenko, A. N., & Volodin, O. A. (2023). Effect of tube rows on two-phase heat transfer characteristics of water over staggered tube bundles under flow boiling mode. *Journal of Thermal Science and Engineering Applications*, 15(5), 050904. https://doi.org/10.1115/1.4056246
- Moreira, D. C., Ribatski, G., & Kandlikar, S. G. (2022). Heat transfer and pressure drop in single-phase flows in tapered microchannels. *Journal of heat transfer*, *144*(7), 072502. https://doi.org/10.1115/1.4054351
- Na, X., Wang, L.-B., Li, H.-R., Lu, X., & Zhang, J.-L. (2025). The correlation between fin side air flow and condensation in inclined tubes of a flat tube bank fin radiator with tube short axis posited horizontally. *International Journal of Thermal Sciences*, 210, 109601.
 - https://doi.org/https://doi.org/10.1016/j.ijthermalsci.2024.109601
- Pope, S. B. (2001). Turbulent flows. *Measurement Science* and *Technology*, *12*(11), 2020-2021. https://doi.org/10.1088/0957-0233/12/11/705
- Sadeghi, M., Yadegari, M., & Khoshnevis, A. B. (2024). Numerical investigation of the flow characteristics around two sequential cylinders with circular and square cross-sections. *Journal of Marine Science and Technology*, 29, 315–332. https://doi.org/10.1007/s00773-024-00987-4
- Sakib, S., & Al-Faruk, A. (2018). Flow and thermal characteristics analysis of plate–finned tube and annular–finned tube heat exchangers for in–line and staggered configurations. *Mechanics and Mechanical Engineering*, 22(4), 1407-1417. https://doi.org/10.2478/mme-2018-0110
- Sang, Y., Li, J., Li, P., Wang, Z., Wan, Z., Jurasz, J., &

- Zheng, W. (2025). Study on optimization and risk resilience of integrated energy system in near-zero carbon park considering carbon taxes. *Energy and Buildings*, 335(15), 115578. https://doi.org/10.1016/j.enbuild.2025.115578
- Sarangi, S., Mishra, D., & Mishra, P. (2020). Parametric investigation of wavy rectangular winglets for heat transfer enhancement in a fin-and-tube heat transfer surface. *Journal of Applied Fluid Mechanics*, 13(2), 615-628. https://doi.org/10.29252/jafm.13.02.30545
- Tang, L., Du, X., Zeng, M. (2017). Effect of inlet angle on the flow performance of elliptical tube fin heat exchangers. *Journal of Power Engineering*, *37*(8), 649-654+672. https://doi.org/10.11949/0438-1157.20190527
- Tsutsui, T. (2010). An experimental study on heat transfer around two side-by-side closely arranged circular cylinders. *Journal of heat transfer*, *132*(11), 111704. https://doi.org/10.1115/1.4002147
- Wang, T. (2018). Numerical simulation of the highpressure gas quenching cooling process and optimization of the air duct structure Chinese Academy of Machinery Science and Technology].
- Wang, Z., Li, X., Tang, L., & Duan,Q. (2019). Optimization study of internal flow guide plates in rectangular section right-angle bent tubes. *Huadian Technology*, 41(8), 32-37. https://doi.org/10.3969/j.issn.1674-1951.2019.08.008
- Wei, L. (2013). Design of key structures for ultra-high pressure gas quenching furnace Tianjin University of Technology].
- Wei, L., Liu, Q., Yang, Y., et al. (2012). An energy-saving finned heat exchanger in a high-pressure gas quenching furnace. *Pressure Vessels*, 29(8), 65-68. https://doi.org/10.3969/j.issn.1001-4837.2012.08.013
- Wu, Z., You, S., Zhang, H., & Zheng, W. (2020). A comparative experimental study on the performance of staggered tube-bundle heat exchanger with unequally-pitch and equally-pitch arrangement in oscillating flow. *International Journal of Heat and Mass Transfer*, 154, 119680. https://doi.org/10.1016/j.ijheatmasstransfer.2020.11
- Yang, D., Wang, N., Xie, J., & Wang, J. (2022). Comparative Numerical Study on Global Heat Transfer Process in Micro-Channel Gas Coolers with Different Structures. *Journal of Applied Fluid Mechanics*, 15(2), 579-589. https://doi.org/10.47176/jafm.15.02.33180
- Yin, L., Jiang, P., Xu, R., & Hu, H. (2020). Water flow boiling in a partially modified microgap with shortened micro pin fins. *International Journal of Heat and Mass Transfer*, 155, 119819. https://doi.org/10.1016/j.ijheatmasstransfer.2020.11 9819

- Zdravkovich, M. (1987). The effects of interference between circular cylinders in cross flow. *Journal of fluids and structures*, *I*(2), 239-261. https://doi.org/10.1016/S0889-9746(87)90355-0
- Zdravkovich, M. (1988). Review of interference-induced oscillations in flow past two parallel circular cylinders in various arrangements. *Journal of Wind Engineering and Industrial Aerodynamics*, 28(1-3), 183-199. https://doi.org/10.1016/0167-6105(88)90115-8
- Zhang, H., & Melbourne, W. (1992). Interference between two circular cylinders in tandem in turbulent flow. *Journal of Wind Engineering and Industrial Aerodynamics*, 41(1-3), 589-600. https://doi.org/10.1016/0167-6105(92)90468-P
- Zhang, L.-Z., Ouyang, Y.-w., Zhang, Z.-G., & Wang, S.-F. (2015). Oblique fluid flow and convective heat transfer across a tube bank under uniform wall heat flux boundary conditions. *International Journal of Heat and Mass Transfer*, 91, 1259-1272. https://doi.org/10.1016/j.ijheatmasstransfer.2015.08.

062

- Zhao, L., Wang, R., Gu, X., & Yang, Z. (2018). Parametric study on rectangular finned elliptical tube heat exchangers with the increase of number of rows.

 International Journal of Heat and Mass Transfer, 126, 871-893.

 https://doi.org/10.1016/j.ijheatmasstransfer.2018.05.036
- Zheng, W., Wang, D., Lyu, F., Shen, Y., Pan, Y., & Wu, M. (2024). Influence of elasticity of high-concentration paste on unsteady flow in pipeline transportation. *Physics of Fluids*, 36(1), 013113. https://doi.org/10.1063/5.0176824
- Zhou, Y., Feng, S., Alam, M. M., & Bai, H. (2009). Reynolds number effect on the wake of two staggered cylinders. *Physics of Fluids*, 21(12), 125105. https://doi.org/10.1063/1.3275846
- Zukauskas, A. A. (1986). Convective heat transfer in heat exchangers. Science Press.